

Nonlinear acousto-magneto-plasmonics

Vasily V. Temnov

IMMM CNRS 6283, Université du Maine, 72085 Le Mans cedex, France
Fritz-Haber-Institut der MPG, Phys. Chemie, Faradayweg 4-6, 14195 Berlin,
Germany

Ilya Razdolski

Fritz-Haber-Institut der MPG, Phys. Chemie, Faradayweg 4-6, 14195 Berlin,
Germany

Thomas Pezeril

IMMM CNRS 6283, Université du Maine, 72085 Le Mans cedex, France

Denys Makarov

Helmholtz-Zentrum Dresden-Rossendorf e. V., Institute of Ion Beam Physics and
Materials Research, 01328 Dresden, Germany

Denis Seletskiy

Department of Physics and Center for Applied Photonics, University of Konstanz,
D-78457 Konstanz, Germany

Alexey Melnikov

Fritz-Haber-Institut der MPG, Phys. Chemie, Faradayweg 4-6, 14195 Berlin,
Germany

Keith A. Nelson

Department of Chemistry, Massachusetts Institute of Technology, Cambridge,
Massachusetts 02139, USA

E-mail: vasily.temnov@univ-lemans.fr

February 2016

Abstract. We review the recent progress in experimental and theoretical research of interactions between the acoustic, magnetic and plasmonic transients in hybrid metal-ferromagnet multilayer structures excited by ultrashort laser pulses. The main focus is on understanding the nonlinear aspects of the acoustic dynamics in materials as well as the peculiarities in the nonlinear optical and magneto-optical response. For example, the nonlinear optical detection is illustrated in details by probing the static magneto-optical second harmonic generation in gold-cobalt-silver trilayer structures in Kretschmann geometry. Furthermore, we show experimentally how the nonlinear

reshaping of giant ultrashort acoustic pulses propagating in gold can be quantified by time-resolved plasmonic interferometry and how these ultrashort optical pulses dynamically modulate the optical nonlinearities. The effective medium approximation for the optical properties of hybrid multilayers facilitates the understanding of novel optical detection techniques. In the discussion we highlight recent works on the nonlinear magneto-elastic interactions, and strain-induced effects in semiconductor quantum dots.

1. Motivation

The main objective of this review is to summarize recent developments in the field of the nonlinear interactions in the magneto-plasmonic and acousto-plasmonic multilayer structures. We are aiming to provide understanding of these fundamental interactions governing the macroscopic properties of the complex multilayer structures excited by femtosecond laser pulses. The role of the ultrashort laser pulses is twofold. On the one hand, high peak intensity is advantageous for efficient excitation of the nonlinear optical processes such as second and third harmonic generation. On the other hand, short laser pulses provide a possibility for an excitation of the electronic, acoustic and magnetic transients as well as allow for sampling of the ensuing dynamics in pump-probe experiments. In addition to application of the external magnetic field, which provides flexible control of the static and dynamic properties in condensed matter systems, in this review we emphasize the high potential that the nanoscale acoustic perturbations offer for study as well as selective dynamic control of various degrees of freedom in complex matter. As we outline below, the functional nanolayers are particularly attractive for these tasks as they support excitation and propagation conditions for ultrashort acoustic pulses while at the same time offer strong sub-micrometer confinement of surface-plasmon-polaritons (SPPs). In turn, macroscopic propagation of SPPs in nanolayers for distances exceeding tens of micrometers makes it possible to enhance the non-linear light-matter interactions in such systems.

A prototypical experimental setup which embodies the concepts outlined above is schematically depicted in Figure 1. Here, a femtosecond pump pulse excites the nanolayer

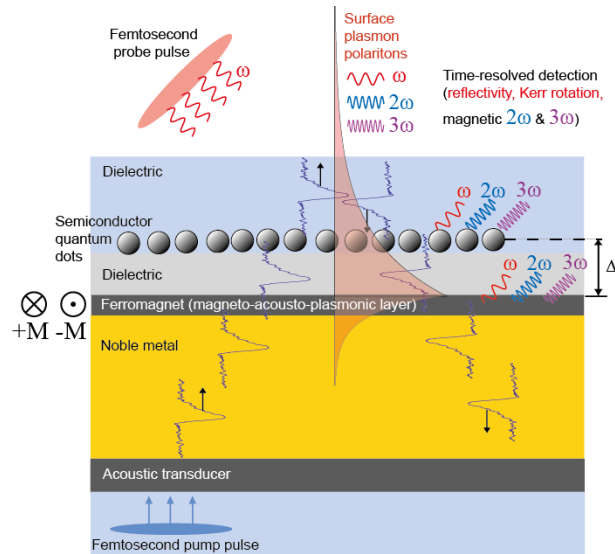


Figure 1. Schematic of a prototypical device for studies of magneto-acousto-plasmonic response of various material systems (e.g. semiconductor quantum dots) under femtosecond excitation and external magnetic field. Ultrafast pump pulse excites a structure made from acoustic transducer, noble metal and a ferromagnet and the ensuing dynamics is probed via various detection methods reviewed here.

structure, which is comprised of an acoustic transducer, noble metal and ferromagnetic layer, while under an optional static magnetic field. Launched magnetic, acoustic and plasmonic transient(s) can be used to study ultrafast dynamics in a system of interest, which is embedded into a dielectric cap layer in close proximity (at a distance Δ) to the metal-dielectric interface [1, 2]. The two examples that we motivate here is the control of the magneto-optical properties in a ferromagnetic compound and time-domain studies of semiconductor quantum dots under strong transient acoustic strain bias at the nanoscale. The response of these systems can be probed via the reviewed detection methods, such as magnetic second harmonic generation (mSHG), time-resolved plasmonic and nonlinear optical (second and third harmonic) probing.

While the device presented in Fig. 1 has not yet been realized, we hope to convince the reader of its great potential for scientific investigations of magneto-acousto-plasmonic interactions in various nanoscale systems. As such, this review provides a progress report on the recent studies which address various isolated components or ideas, comprising potential building blocks toward our envisioned device.

The presented material is divided into several sections. Section two discusses two experimental geometries used to excite surface plasmon polaritons in magneto-plasmonic multilayers: Kretschmann configuration for a thin multilayer on a dielectric prism and the plasmonic interferometry for macroscopically thick all-metallic samples.

Section three describes some recent advances in the linear and nonlinear magneto-plasmonics. A weak external magnetic field is shown to induce large modulation in the intensity of surface second harmonic generation (SHG) and also to identify the role of surface plasmon polaritons in the nonlinear frequency conversion phenomena. The effective medium approximation for magneto-plasmonic metal-ferromagnet multilayer structures helps to understand the results. A phenomenological model based on the interference between the magnetic and nonmagnetic contributions from two effective interfaces is developed to explain the observations.

Section four discusses generation and characterization of giant and ultrashort acoustic pulses in (noble metal)-ferromagnet bilayer structures and evidences their impact on the SHG output. Another phenomenological model based on the acoustic modulation of the optical properties of a thin ferromagnetic layer is proposed to explain the experimental observations.

Section five concerns the specificity of the sample fabrication for plasmonic and acoustic measurements.

In the discussion section we outline other involved phenomena, notably related to ultrafast magnetization dynamics, thermal effects and strain effects in semiconductor quantum dots.

2. Optical spectroscopy with surface plasmon polaritons

Time-dependent perturbations of electron density distribution in metals are at the heart of plasmonics. The relaxation dynamics is governed by oscillations of the electrons at the so-called plasma frequency, which, in the long-wavelength limit of free-electron approximation, is given by $\omega_p = \sqrt{\frac{n_e e^2}{\epsilon_0 m}}$, where n_e , e and m are the electronic density, charge and mass, respectively and ϵ_0 is the dielectric permittivity of free space. Since in most metals there is at least one free electron per ion, the resulting electron plasma density is very high, $n_e \sim 10^{22} \text{ cm}^{-3}$, with a corresponding ω_p in the visible to ultraviolet frequency range. Optical fields at frequency $\omega < \omega_p$ are effectively screened by the plasma, resulting in a penetration profile which is exponentially attenuated within the so-called *skin depth* δ_{skin} . For the majority of metals the skin depth lies in the range of 10-20 nm in the visible and near-infrared frequency range. A Drude model provides the dielectric response function of free electrons $\epsilon_m(\omega) = 1 - \omega_p^2/(\omega(\omega + i/\tau_c))$, where τ_c stands for an effective electron scattering time. This simple expression offers a reasonable approximation for the optical properties of free-carrier-like metals (Al, Ag, Au, Cu) used in plasmonics because of their small losses (large τ_c).

In low-dimensional metallic nanostruc-

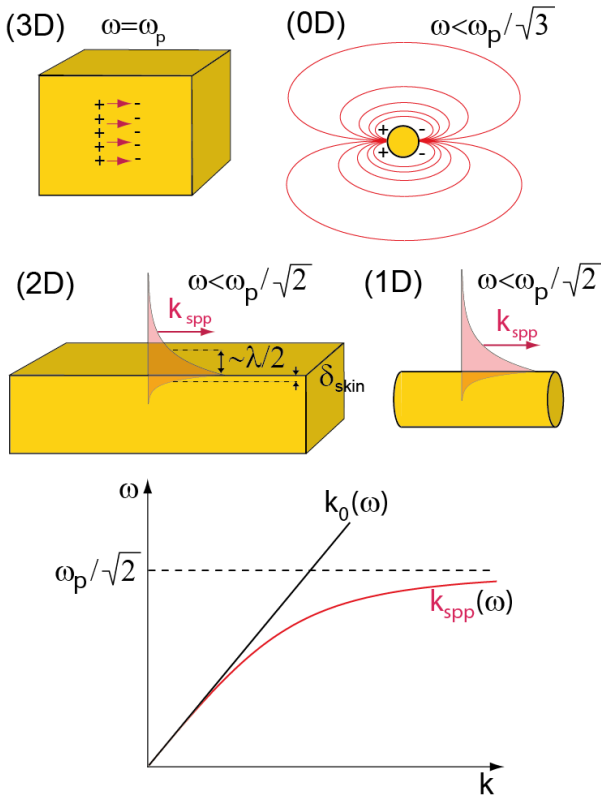


Figure 2. Frequency of oscillations of electron gas in bulk metal (3D), is modified by surface effects in metallic nanoparticles (0D), nanowires (1D) and surfaces (2D). Whereas metallic nanoparticles possess a specific, localized surface plasmon (LSP) resonance frequency determined by their geometry, surface plasmon polaritons (SPPs) in 1D and 2D form a broad frequency band $\omega(k_{\text{spp}})$ and may propagate over macroscopic distances while obeying a characteristic dispersion relation.

tures such as metal surfaces (2D), wires (1D) or dots (0D), the frequency of plasma oscillations is substantially affected by charge separation at the surface. This is illustrated in Fig. 2 which shows the different plasma frequencies and mixed electromagnetic/surface charge density excitations in various geometries.

In the case of zero-dimensionality (0D), the electron gas oscillates at a fixed resonance frequency and may lead to significant enhancement of optical fields close to the surface of

the nanoparticle due to the nanoantenna effect. This field enhancement is of key importance to understanding the interaction mechanisms between plasmonic nanoparticles and nano-scale light emitters. The resonance frequency for metal nanoparticles of the diameter smaller than the skin depth δ_{skin} tends to a value of $\omega_p/\sqrt{3}$, while with the increased diameter it experiences a red shift [3]. By varying the diameter of 0D metallic nanoparticles ranging from a few to tens of nanometers, this localized plasmon frequency can be tuned over the entire visible spectral range.

In addition to the bulk and the localized plasmon modes, surface plasmon modes can be supported at one or two dimensional interfaces. These collective excitations are often referred to as surface plasmon polaritons. These are coupled electromagnetic - surface charge density waves on flat metal surfaces and wires which can propagate over macroscopic distances, largely exceeding the optical wavelength λ . In the case of metallic surface, the electromagnetic fields in the direction normal to the interface are exponentially bound. On the vacuum side, the typical exponential decay length is a fraction of λ , therefore resulting in strong sub-wavelength field confinement. Inside the metal, the intensity of electric and magnetic components of the electromagnetic field decays exponentially within the skin depth. SPPs exist in a broad frequency band below the cut-off frequency $\omega_p/\sqrt{2}$ and are characterized by dispersion relation $\omega(k_{\text{spp}})$, where k_{spp} is the wave vector of the surface plasmon (lower panel in Fig. 2). This dispersion relation is identical for 1D and 2D cases, as long as the nanowire radius significantly exceeds the skin depth [4] and is given by $k_{\text{spp}}(\omega) = k_0(\omega)\sqrt{\frac{\epsilon_m(\omega)}{\epsilon_m(\omega)+1}}$, where $k_0(\omega) = \omega/c$ is the wave vector of light in vacuum.

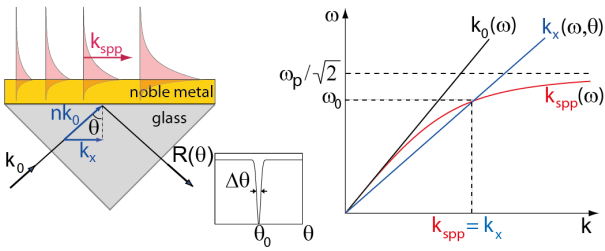


Figure 3. Illumination of a thin (noble) metal film through the glass prism (known as Kretschmann geometry [5]) supports the conditions for excitation of the surface plasmon polariton modes. SPP excitation at the metal-air interface is manifested by a sharp minimum in the reflectivity $R(\theta)$, once the light is made incident at specific angle of θ_0 of the SPP excitation condition. The condition is satisfied at the intersection point of the dispersion relations of the light and surface plasmon modes ($k_{\text{spp}}(\omega_0) = k_x(\omega_0, \theta_0)$ on the right panel), resulting in strong electric field enhancement at the surface.

The details of the coupling of the surface plasmon modes and optical fields in low-dimensional structures are worth further consideration. Due to the localized nature of the 0D resonance, plasmonic response of the metallic nanoparticles can be effectively approximated as a Hertzian dipole, where large spatial bandwidth of the possible wave vectors manifests in direct coupling plane electromagnetic waves. The situation is entirely different for surface plasmon polaritons in 1D and 2D geometries. Since their dispersion curve $\omega(k_{\text{spp}})$ never crosses the light line in vacuum ($k_{\text{spp}} > k_0$ for all frequencies), they cannot be excited by plane electromagnetic waves impinging on a metal-air interface. An elegant and most widely used way to excite SPP modes is provided by the so-called Kretschmann geometry (see Fig. 3), where a thin metal film deposited on top of a dielectric prism is illuminated by a collimated light beam through the prism with refractive index $n > 1$. For a particular combination of the incident angle θ_0 and light frequency ω_0 , the in-plane com-

ponent of the wave vector of incident light $k_x(\omega, \theta) = n(\omega)k_0(\omega) \sin \theta$ matches the wave vector of a surface plasmon polariton:

$$k_{\text{spp}}(\omega_0) = n(\omega_0)k_0(\omega_0) \sin \theta_0. \quad (1)$$

In case of a monochromatic laser source, the angular dependence of reflectivity $R(\theta)$ shows a sharp dip at $\theta = \theta_0$ indicating that a significant fraction of incident energy is converted into the SPP mode, propagating along the metal-air interface. The metal layer should be relatively thin (typically ~ 50 nm) in order to allow for efficient coupling of the incident light from the glass-metal to the metal-air interface. Thicker films would decrease the coupling efficiency due to enhanced attenuation of the evanescent wave in metal whereas in even thinner films the hybridization of the SPPs at the two interfaces and the subsequent formation of symmetric and antisymmetric modes would introduce additional radiative losses [6]. Upon satisfaction of the SPP excitation condition, the intensity of the excited SPP mode grows with propagation along the illuminated region of the surface and can get up to 300 times larger as compared to the incident wave, limited by the ohmic losses in the metal film [7, 8]. In practice, this field enhancement is lower due to parasitic effects which reduce the surface plasmon propagation length such as, for example, surface roughness and material inhomogeneities [9]. In hybrid ferromagnet-(noble metal) multilayer structures the field enhancement is further reduced due to SPP absorption in a ferromagnet.

Scattering of the incident light on natural or artificial surface defects, with a size of the order of a wavelength or smaller, represents another common way to satisfy the condition for SPP excitation [11]. A pair of appropriately-spaced sub-wavelength

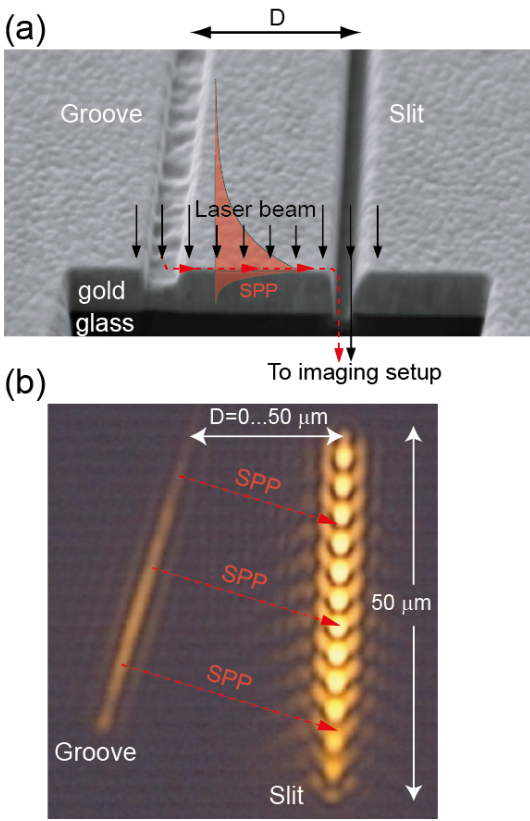


Figure 4. Plasmonic microinterferometer based on a tilted slit-groove pair. (a) SEM micrograph showing a typical depth profile of the slit-groove structure (slit-groove distance D of $1 \mu\text{m}$, slit-groove tilt angle of 3° , slit width 100 nm , groove width 200 nm , groove depth 100 nm) milled into a 200 nm -thick gold film on a glass substrate by a focused ion beam. (b) False-color image of optical transmission of a homogeneously illuminated microinterferometer in a near-infrared, with a minimum slit-groove spacing of $D = 20 \mu\text{m}$ and slit-groove tilt angle of 15° . The periodic modulation of light intensity transmitted through the slit is due to interference with surface plasmons launched by the groove (see text for details). Adopted with permission from Ref. [10].

defects can serve for in- and outcoupling of the incident light to the SPP modes and producing the plasmonic interference fringes [12, 13, 14].

Figure 4(a) shows a scanning electron microscope (SEM) micrograph of the plasmonic microinterferometer, which consists of a slit-groove pair milled into a 200 nm gold film with a 30 kV Ga^+ focused ion beam. The

200 nm gold film was grown by magnetron sputtering on a 2 nm -thin chromium buffer layer on a glass substrate. The length of both the slit and the groove is $50 \mu\text{m}$. The slit has a width of 100 nm and extends through the thickness of the gold layer to the glass substrate. The depth of the groove is 100 nm and it is 200 nm wide. A series of similar structures was fabricated, where the slit-groove tilt angle was systematically varied between 3° and 15° and the slit-groove distance between 0 and $50 \mu\text{m}$. If the whole area of the microinterferometer is homogeneously illuminated with coherent light, the SPP, first launched at the groove, will propagate toward the slit and interfere with the directly transmitted light upon outcoupling back into the light mode. An optical transmission image of a slit-groove microinterferometer, illuminated by a collimated p-polarized laser beam (beam waist $\sim 40 \mu\text{m}$ FWHM, $\lambda = 800 \text{ nm}$) under nearly normal incidence, is shown in Fig. 4(b). A bright periodic intensity modulation of light transmitted through the slit represents the plasmonic interference pattern. A small tilt angle between the slit and the groove determines the spatial periodicity of interference fringes and allows for interferometric measurements at a single wavelength with a single microinterferometer.

The interferometric sensitivity to the phase shift acquired by the SPP upon macroscopic propagation of the distance between the groove and the slit can be harnessed for sensing. In the hybrid multilayers, the phase and/or the contrast of these plasmonic interference fringes can be conveniently controlled via the modulation of the dielectric susceptibility by means of either magneto-optical effects in magneto-plasmonics or elasto-optical effects in acousto-plasmonics.

3. Magneto-plasmonics

3.1. Linear magneto-plasmonics

The influence of the external magnetic field on plasmonic properties is extensively discussed elsewhere [15]. The magnetic field control of the plasmonic properties has been demonstrated in a number of systems [16, 17, 18, 19, 20, 21, 22, 23, 24, 25]. Here we shall focus on the properties of the SPPs in a hybrid (noble) metal-ferromagnet-(noble) metal multilayer structure, which serves as a robust playground for magneto-plasmonics (Fig. 5). The geometry of SPPs at 800 nm wavelength in a Au-Co-Au multilayer structure is shown in Fig. 5(a). Both the real and imaginary parts of the complex SPP wave vector can be calculated within the effective medium approximation [26, 27]. The effective dielectric function

$$\varepsilon_{\text{eff}} = \frac{1}{\delta_{\text{skin}}} \int_0^{\infty} \varepsilon(z) e^{-z/\delta_{\text{skin}}} dz, \quad (2)$$

accurately reproduces the SPP dispersion relation in a magneto-plasmonic multilayer structure

$$k_{\text{spp}} = k_0 \sqrt{\frac{\varepsilon_{\text{eff}}}{1 + \varepsilon_{\text{eff}}}}. \quad (3)$$

The validity of this approximation is illustrated by the dependence of SPP propagation length $L_{\text{spp}} = 1/(2\text{Im}[k_{\text{spp}}])$ in a Au-Co-Au multilayer, where the 6 nm-thick cobalt layer was placed at a variable depth h below the gold-air interface (Fig. 5(b)). A good quantitative agreement between the effective medium approximation and exact transfer-matrix calculations [29] is obtained. Observation of significant decrease of the SPP propagation length L_{spp} for small values of h is attributed to additional ohmic losses introduced when the ferromagnetic layer is in a non-negligible overlap with the spatial envelope of the intensity profile associated with the SPP mode. The

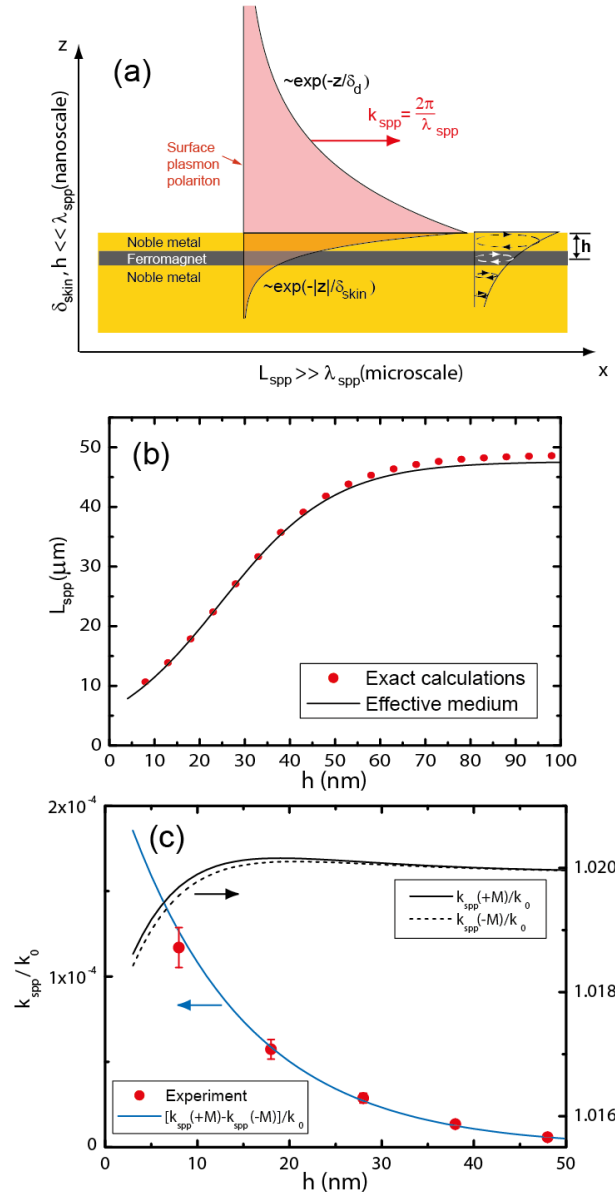


Figure 5. (a) SPPs in metal/ferromagnet/metal multilayer structures possess the spatial distribution of the in-plane electric field (shaded area shows $|E_z(z)|^2$), which is almost identical to that for a single metal film. Dashed elliptical contours represent the shape of the SPP electric field driving the motion of the electrons. (b) The dependence of the SPP decay length L_{spp} on the location h of the cobalt layer beneath the gold-air interface, showing excellent agreement with an effective medium approximation fit (black line). (c) In-plane magnetization reversal (in y -direction) in ferromagnetic cobalt changes the SPP wave vector $k_{\text{spp}}(\pm M)$. Its magnetic modulation $k_{\text{spp}(+M)} - k_{\text{spp}(-M)}$ obtained within the effective medium approximation is in agreement with experimental measurements from Ref. [26]. Figure (a) adopted with permission from Ref. [28].

influence of a thin ferromagnetic layer on the skin depth δ_{skin} is negligibly small and one can safely use its value for SPPs propagating at the noble metal-dielectric interface.

The effective medium approximation provides an adequate description of the dependence of SPP wave vector on the magnetic field as well. Assuming that the effective magneto-optical tensor is given by:

$$\hat{\epsilon}_{\text{eff}}(\pm M) = \begin{pmatrix} \epsilon_{\text{eff}} & 0 & \pm \epsilon_{\text{eff}}^{xz} M \\ 0 & \epsilon_{\text{eff}} & 0 \\ \mp \epsilon_{\text{eff}}^{xz} M & 0 & \epsilon_{\text{eff}} \end{pmatrix}, \quad (4)$$

where M denotes the y -component of magnetization vector normalized to its saturation value and the nondiagonal components are given by

$$\epsilon_{\text{eff}}^{xz} = \frac{1}{\delta_{\text{skin}}} \int_0^\infty \epsilon^{xz}(z) e^{-z/\delta_{\text{skin}}} dz, \quad (5)$$

we obtain the following dispersion relation for SPPs [30]:

$$k_{\text{spp}}(\pm M) = k_0 \sqrt{\frac{\epsilon_{\text{eff}}}{1 + \epsilon_{\text{eff}}}} \left(1 \pm \frac{i \epsilon_{\text{eff}}^{xz} M}{(1 - \epsilon_{\text{eff}}^2) \sqrt{\epsilon_{\text{eff}}}} \right). \quad (6)$$

For a special case of a ferromagnet (FM) layer with thickness h_1 sandwiched between two layers of a noble metal, the effective medium approximation for the non-diagonal dielectric susceptibility component gives

$$\epsilon_{\text{eff}}^{xz} \simeq \frac{h_1}{\delta_{\text{skin}}} \epsilon_{\text{(FM)}}^{xz} e^{-h/\delta_{\text{skin}}} \quad (7)$$

resulting in the following magneto-plasmonic modulation of SPP wave vector Δk_{mp} :

$$\Delta k_{\text{mp}} \simeq i \epsilon_{\text{(FM)}}^{xz} M \frac{2h_1 \epsilon_{\text{eff}} k_0^2}{(1 + \epsilon_{\text{eff}})(1 - \epsilon_{\text{eff}}^2)} e^{-h/\delta_{\text{skin}}}, \quad (8)$$

where we have introduced the magnetic modulation of SPP wave vector $2\Delta k_{\text{mp}} = k_{\text{spp}}(+M) - k_{\text{spp}}(-M)$ and used the expression for SPP skin depth $\delta_{\text{skin}} = \frac{1}{2k_0} \text{Im} \frac{\sqrt{1 + \epsilon_{\text{eff}}}}{\epsilon_{\text{eff}}}$. It is remarkable that this result is identical to the analytical expression obtained from transfer-matrix calculations for the limit of an infinitely thin ferromagnetic layer [26, 29].

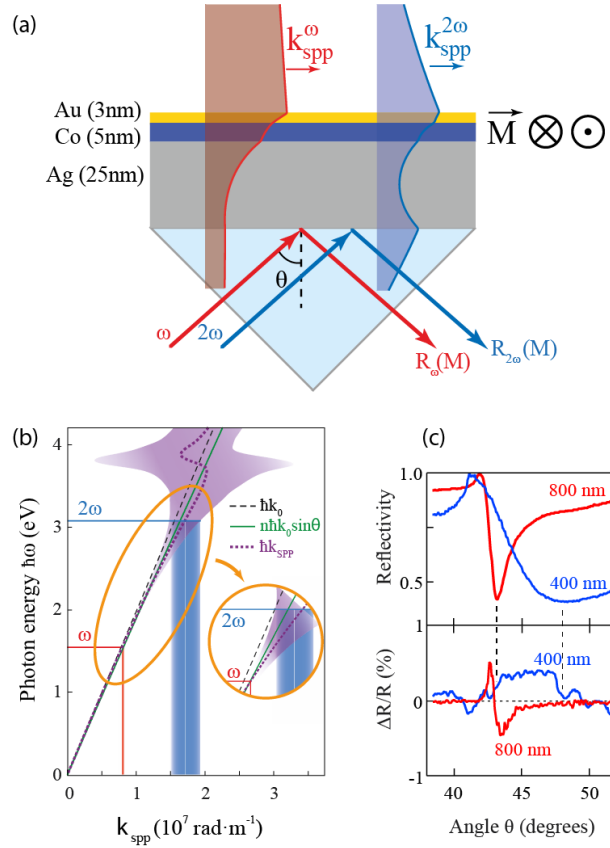


Figure 6. (a) Surface plasmons in thin Au/Co/Ag multilayer structures: the spatial distribution of the squared tangential projection of SPPs-electric field at the fundamental ω and double 2ω frequencies at their resonant angles. (b) Dispersion of the SPP in the Au/Co/Ag trilayer under study. Black dash and green solid lines represent the photon dispersion in vacuum and in glass, respectively. Thick dot purple line is the calculated SPP dispersion, its linewidth is shown with the purple background area. The inset illustrates the possibility of a simultaneous excitation of the SPPs at both frequencies ω and 2ω . (c-d) Linear-optical reflectivity R and magnetization-induced reflectivity variations $\Delta R/R = [R(+M) - R(-M)]/[R(+M) + R(-M)]$ for the excitation with the 800 nm and 400 nm wavelength. Figure adopted with permission from Ref. [27].

The developed approach appears to be useful not only in the interferometric measurements with SPPs, but also in the conventional Kretschmann geometry. In a Au/Co/Ag multilayer the SPP resonance can be excited at both 800 nm and 400 nm wavelengths,

Fig. 6(a). The SPP dispersion in Fig. 6(b) is displayed by the shaded area where the width is proportional to SPP damping (imaginary part of SPP wave vector), which strongly increases when approaching the blue part of the visible spectral range. Whereas SPP dispersion results in the shift of the SPP resonance angle θ_0 for 400 nm light (as compared to 800 nm), the increased damping makes the Kretschmann reflectivity dip much broader (Fig. 6(c)).

The effect of the external magnetic field is the same for both frequencies and leads to a small shift of the resonance angles upon magnetization reversal. The positions of the Kretschmann reflectivity minima precisely correspond to the zeros on magneto-plasmonic modulation curves, confirming the physical interpretation suggesting that the magneto-plasmonic modulation of SPP wave vector should result in an angular shift of the reflectivity minima.

Here we would like to note that the reflectivity minimum in Kretschmann configuration cannot always be attributed to the excitation of SPPs. Depending on the direction of the energy flow in a thin metal film, i.e. from bottom to the top (Kretschmann configuration) or from top to the bottom (plasmonic interferometry, Otto configuration), the dispersion of surface electromagnetic waves obeying the boundary conditions may be different. The difference between the conventional SPP modes and the so-called perfectly absorbed (PA) mode has been experimentally observed only very recently [31]. In the forthcoming discussion of the nonlinear magneto-plasmonic response we leave the question about the nature of the mode at the frequency 2ω , i.e. whether SPP or PA open.

As we are going to show in the forthcoming sections, the effective medium approx-

imation for SPPs, which was originally introduced in the linear magneto-plasmonics, appears to be particularly useful in description of nonlinear magneto-plasmonics and acousto-plasmonics.

3.2. Nonlinear magneto-plasmonics

Nonlinear magneto-plasmonics is a relatively young field of magneto-photonics, which utilizes SPP excitations for tailoring the magnetization-induced contributions to the nonlinear-optical response of systems. The motivation for the emergence of this field of research is essentially twofold. First, as compared with nonlinear plasmonics [14, 32, 33], magnetic field conveniently offers a universal tool for controlling the nonlinear-optical response. Second, nonlinear magneto-optical effects are much stronger as compared to their linear counterparts, where magnetization-induced effects stay relatively small despite of being enhanced by SPPs [34, 27].

As it has been discussed in the previous section, in linear magneto-plasmonics the magnetic effects in the transversal Kerr geometry (magnetization is perpendicular to the incidence plane) are usually ascribed to the magnetization-induced modulation of SPP wave vector k_{spp} . However, in the nonlinear magneto-optics the response is more complex. In what follows, we shall restrict our considerations of nonlinear optical effects to second harmonic generation (SHG) only, although the general principles of nonlinear magneto-plasmonics also apply to other effects such as difference frequency (often in THz domain), third harmonic generation, etc. Here we focus on the advantages of the SPP-induced second harmonic generation in magnetic media, including both enhancement

of the magnetic effects and unraveling new SPP-assisted mechanisms to control optical nonlinearities.

One of the basic nonlinear-optical processes, SHG is governed by the second-order nonlinear-optical susceptibility tensor $\chi^{(2)}$. Various mechanisms of the anharmonicity in the optical response to electromagnetic field $E(\omega)$ lead to the emergence of nonlinear polarization, which, at the lowest second order, occurs at the double frequency 2ω [35]:

$$P_i(2\omega) = \chi_{ijk}^{(2)}(-2\omega; \omega, \omega) : E_j(\omega)E_k(\omega). \quad (9)$$

This polarization then emits an electromagnetic wave. One of the key properties of the $\chi^{(2)}$ tensor is its strong sensitivity to the inversion symmetry. It can be shown that dipolar $\chi^{(2)}$ vanishes in the centrosymmetric media such as, for instance, bulk metals. In such systems efficient SHG is generated predominantly at the interfaces, where the inversion symmetry is broken. The renowned SHG sensitivity to the interfacial properties of media is advantageous for plasmonics with SPPs. Under resonant excitation conditions in Kretschmann configuration SPPs boost up the local electromagnetic fields and can strongly enhance the SHG output [36]. In certain cases it is also convenient to take into account the influence of SPPs in the form of a resonant contribution to the $\chi^{(2)}$ -tensor [35, 37]. Importantly, since $\chi^{(2)}(-2\omega; \omega, \omega)$ is sensitive to resonances (of various nature) not only at the fundamental ω , but also at the double frequency 2ω , SPPs at both of these frequencies contribute to the SHG output [38, 39].

Within this formalism, the magnetization-induced modulation of the SHG output is described in the following way. In magnetized media, the magnetization-dependent $\chi^{(2)}$ tensor can be represented as a sum of the non-magnetic (crystallographic) $\chi^{(2)}$ and

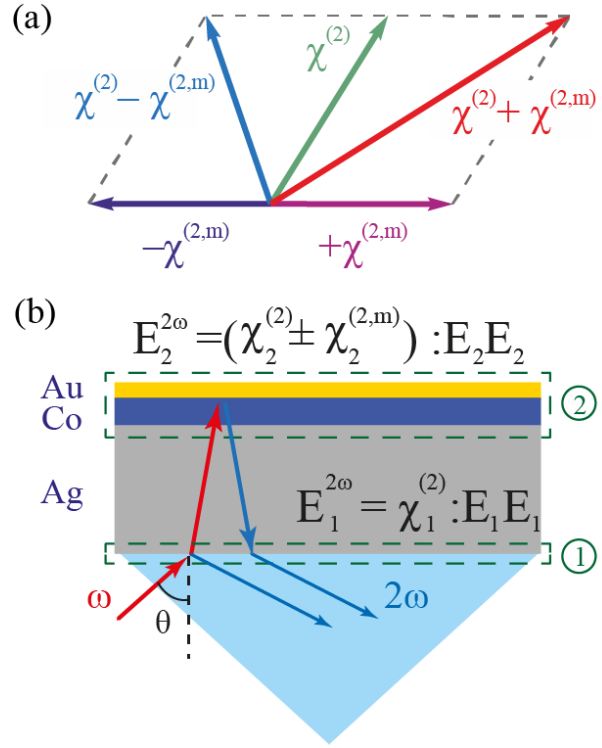


Figure 7. (a) Illustration of the origin of the inequality of the SHG intensities for the opposite direction of the magnetization M leading to the non-zero magnetic SHG contrast $\rho_{2\omega}$. The sign of the magnetic contribution to the nonlinear susceptibility $\pm\chi^{(2,m)}$ is flipped when the magnetization is reversed. (b) Magnetic SHG generation in a multilayer structure excited in Kretschmann geometry: SHG sources at the two interfaces, bottom (1, glass/Ag) and top (2, air/Au/Co/Ag) within the effective interface approach.

magnetization-induced $\pm\chi^{(2,m)}$ contributions [40]. The latter changes sign upon reversing the magnetization, whereas the interference of these two contributions results in a magnetization-induced modulation of the SHG intensity (Fig. 7(a)). The magnitude of the effect can be conveniently characterized by the so-called magnetic SHG (mSHG) contrast $\rho_{2\omega}$:

$$\rho_{2\omega} = \frac{I_{2\omega}(+M) - I_{2\omega}(-M)}{I_{2\omega}(+M) + I_{2\omega}(-M)}, \quad (10)$$

where $I_{2\omega}(+M)$ and $I_{2\omega}(-M)$ are the SHG intensities measured for the two opposite directions of magnetization. It should be

noted that in a complex multilayer system, where multiple SHG sources are located at each interface, the rigorous description of the SHG output becomes increasingly complicated. Instead, a rather simple approach of the effective interface can be introduced, where a stack of thin metallic layers is replaced by a single SHG source (Fig. 7(b)). Within this approach, the role of SPP excitation in altering the magnetization-induced effects in SHG can be considered twofold. Upon such an excitation, either the relative magnitude of the $\chi^{(2)}$ contributions or the relative phase between them can be modulated. The former, realized by Krutyanskiy *et al.* [41] relies on the tensorial nature of $\chi^{(2)}$. Here, the crystallographic and magnetic SHG contributions are provided by the different projections of the fundamental field $E(\omega)$. These projections experience unequal SPP-assisted enhancement resulting in a modulation of the magnetization-induced SHG output. The second option [42, 43] highlighted the importance of the SPP-induced variations of the phase of the electromagnetic field. The physical origin of such phase modulations beyond the usual field enhancement remains largely unexplored.

A number of systems has been successfully investigated with nonlinear magneto-plasmonics. We note that nonlinear magneto-optics of nanoparticles and planar nanostructures [44, 45, 46, 47] supporting localized surface plasmon resonances are beyond the scope of this work. The most straightforward approach utilizing SPP excitation at the interface of a ferromagnetic (Fe, Co, Ni) rather than conventional plasmonic (Al, Ag, Au, Co) metals faces a few challenges. Apart from dealing with overdamped plasmonic excitations ($L_{\text{spp}} < \lambda_{\text{spp}}$), these metals possess a relatively low second-order nonlinear-

ity usually attributed to the localized d -band electrons. Nevertheless, magnetic SHG studies both on periodically perforated films [42] and in Kretschmann geometry [48] demonstrated significant SPP-assisted modulation of the magnetic contrast $\rho_{2\omega}$. In the systems discussed above, the incident electromagnetic wave excited SPPs at the fundamental frequency ω and the plasmonic enhancement of the local electromagnetic field $E(\omega)$ boosted the efficiency of the nonlinear-optical conversion.

Multilayer structures consisting of a ferromagnetic layer sandwiched between the two layers of noble metals offer a considerable expansion of opportunities in nonlinear magneto-plasmonics. For example, photons initially up-converted (frequency-doubled) at the interfaces can excite SPPs at 2ω and thus contribute to the enhancement of the SHG output [39, 49]. This mechanism requires the sample to support propagating SPP modes at the double frequency 2ω and imposes additional requirements on the system. It can be especially challenging in the case of SPP excitation on periodically corrugated surfaces, where the spatial periodicity was designed to achieve resonant conditions for SPP excitation at the fundamental frequency ω only. Another impairing factor is related to increased optical losses caused by the spectral overlap of SPP at 2ω with interband transitions, which is the case for Au at photon energies above 2.4 eV. This shifts the focus of attention toward other plasmonic metals such as Al or Ag which are capable of sustaining SPPs across the whole visible spectral range.

In the following we discuss a showcase of the proposed nonlinear magneto-plasmonic mechanism where a significant improvement of the magnetization-induced modulation reaching up to 33% has been achieved. We con-

sider a thin gold/cobalt/silver trilayer grown on a glass substrate by means of the magnetron sputtering. A 5 nm-thin magneto-optically active layer of ferromagnetic cobalt was protected from oxidation by a 3 nm-thin layer of gold. A 25 nm-thick silver layer acted as the main constituent in this hybrid plasmonic nanostructure, which was excited by collimated 100 fs short laser pulses through the glass prism. The reflected SHG intensity was recorded as a function of the incidence angle θ for the two opposite directions of magnetization in cobalt in the transverse Kerr geometry (see Fig. 8(a)).

Due to the inevitable dispersion, the SPP excitations at fundamental and double frequencies in Kretschmann geometry occur at slightly different angles. However, nonlinear-optical considerations discussed above suggest a possibility of nonlinear phase-matching between the second harmonic SPP at the gold-air interface with the k -vector $k_{\text{spp}}^{2\omega}$ and the excitation source at the silver-glass interface characterized by the in-plane component of the k -vector $n(\omega)k_0(\omega)\sin\theta$. This phase-matching occurs at an angle θ_{nl} given by:

$$k_{\text{spp}}^{2\omega} = 2n(\omega)k_0(\omega)\sin\theta_{\text{nl}}, \quad (11)$$

Being just one of several possible SPP frequency conversion pathways [49, 50], this phase-matching condition is of paramount importance as it determines the resonant SPP-induced enhancement of the nonlinear susceptibility $\chi^{(2)} = \chi_{\text{nr}}^{(2)} + \chi_{\text{res}}^{(2)}(\theta)$ with SPP-mediated resonant contribution [35, 37]:

$$\chi_{\text{res}}^{(2)}(\theta) \propto \frac{1}{\theta - \theta_{\text{nl}} + i\Gamma} \quad (12)$$

with $\Gamma = \text{Im}[k_{\text{spp}}^{2\omega}]/(k_0(\omega)n(\omega))$.

Whereas the linear reflectivity at both frequencies ω and 2ω shows only small modulations of the order of 1%, as discussed in the previous section (Fig. 6(c)), the angular

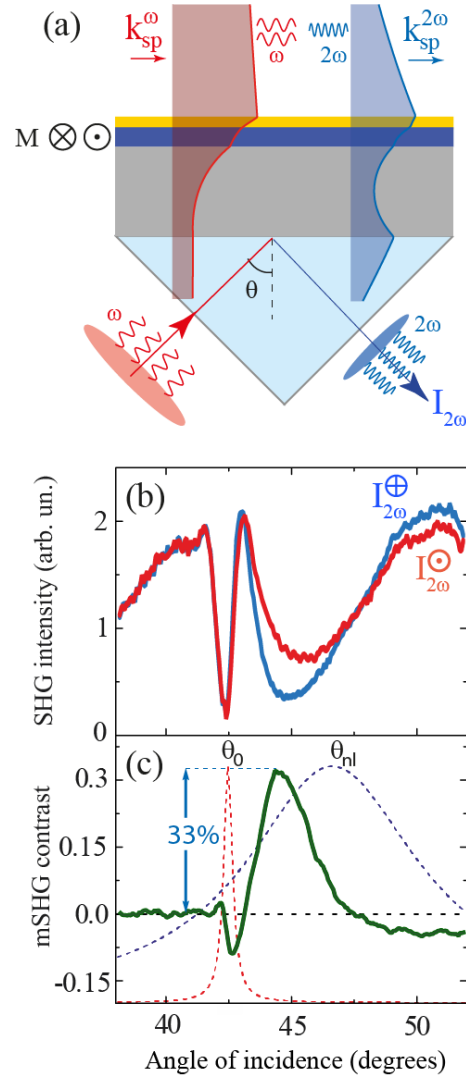


Figure 8. (a) Schematic of the SPP-induced magnetic SHG in Kretschmann geometry. The shaded areas represent the calculated distributions of the square of the SPP electric field $|E_z|^2$. A noticeable field enhancement at the air/Au interface indicates that the SPPs at both ω and 2ω are excited. Angular dependence of (b) the SHG intensity for the two opposite directions of magnetization in Co (red and blue) and (c) mSHG magnetic contrast (green). Red and blue dashed lines represent the SPP resonance lines for the 800 nm pump wavelength (described by Eq. (1)) and the nonlinear (SHG) excitation at 400 nm wavelength (according to Eq. (11), respectively). Note that the maximum of mSHG contrast is located between fundamental and the nonlinear (SHG) SPP resonances.

dependence of the nonlinear SHG spectra in Fig. 8(b) displays drastic changes. Contrary to the previously reported results on a gold film [39], the angular positions of SPP resonances for the fundamental and SHG frequencies in our multilayer structure correspond to the pronounced minima in the SHG intensity. A strong dependence of the total SHG intensity on the magnetization direction $I_{2\omega}(\pm M)$ is quantified by the magnetic SHG contrast $\rho_{2\omega}$ shown in Fig. 8(c).

It is seen that the largest magnetisation-induced modulation of the SHG intensity is accompanied by the SPP excitation at the SHG frequency and not the fundamental one. Angular dependence of mSHG contrast displays a large modulation amplitude reaching 33 % at $\theta = 44$ degrees. The data for other excitation wavelengths can be found elsewhere [27]. For the shortest wavelength (760 nm) the mSHG maximum is only about 20%, since in this case the SPP damping at the SHG frequency becomes so large that the system approaches the region with the non-propagating (overdamped) SPPs.

Note that the mSHG contrast at the fundamental SPP resonance is barely reaching 10%. This observation is in line with the most recent results by Zheng *et al.* [48], who reported similar values of the mSHG contrast on a 10 nm-thin iron film on glass, as well as with the results by Pavlov *et al.* [51] obtained on Au/Co/Au multilayer, the structures not supporting SPPs at the SHG frequency. This fact, along with the dispersive shift of mSHG maximum reinforces our conclusion that the 33 % large mSHG contrast (which is equivalent to the increase of the SHG intensity by a factor of 2 upon magnetization reversal) is dominated by the nonlinear SPP resonance at the SHG frequency.

Following Palomba and Novotny [39],

the complex angular dependence of the SHG intensity from a thin gold film on glass is explained by an interference of two contributions coming from the metal-air and metal-glass interfaces. In our case (Fig. 7(b)) the silver-glass interface acts as a source of the nonmagnetic SHG $\vec{E}_1^{2\omega}$, and the upper part consisting of Au and Co layers is assumed to generate the electric field $\vec{E}_2^{2\omega}$ containing both magnetic $\chi^{(2m)}$ and non-magnetic $\chi^{(2)}$ contributions. Thus the total SHG intensity $I_{2\omega}$ is described by:

$$\begin{aligned} I_{2\omega} &\propto |\vec{E}_1^{2\omega} + \vec{E}_2^{2\omega} \pm \vec{E}_{2m}^{2\omega}| = \\ &= |\chi_1^{(2)} : \vec{E}_1 \vec{E}_1 + (\chi_2^{(2)} \pm \chi_2^{(2m)}) : \vec{E}_2 \vec{E}_2|^2 \end{aligned} \quad (13)$$

Here the complex tensor components $\chi_1^{(2)}$ and $\chi_2^{(2)} \pm \chi_2^{(2m)}$ represent the effective optical nonlinearities at both interfaces. Owing to the resonant $\chi_{\text{res}}^{(2)}$ contribution, the SHG field enhanced at the top interface destructively interferes with the one generated at the bottom interfaces, which explains the experimentally observed SHG intensity minima. Within this approach, using Eq. (13) and assuming the resonant $\chi_{\text{res}}^{(2)}$ given by Eq. (12) we were able to fit the experimental angular spectra of both SHG intensity and magnetic contrast [27]. The frequency dependence over the dispersive SPP spectral range revealed that the maximum value of 33% mSHG contrast remained constant whereas its angular width decreased as the nonlinear SPP resonance became narrower (Γ decreased) and shifted towards the fundamental one. As such, the dominant role of the nonlinear SPP resonance in Kretschmann geometry, which is responsible for the increase of the mSHG magnetic contrast, was identified.

In conclusion, the nonlinear magneto-plasmonics offers a strong enhancement of the magnetization-induced effects as compared to its linear counterpart. In the given spectral

range one would expect to reach further enhancement of mSHG contrast by systematically varying the individual thicknesses in this trilayer structure.

4. Acousto-plasmonics

4.1. Linear acousto-plasmonics

In previous sections we have investigated stationary properties of metal-ferromagnet multilayer structures. Femtosecond light pulses were used to achieve high peak intensities of electromagnetic radiation facilitating efficient nonlinear optical frequency conversion. However, irradiation of metallic samples with femtosecond optical pulses is known to trigger the complex dynamics of electronic, acoustic and magnetic excitations [52, 53, 54, 55]. In this section we will discuss transient effects of ultrashort acoustic pulses on SPPs.

Among different mechanisms of acoustic generation the so-called thermo-elastic mechanism is the most common one [56, 57]. Absorption of light leads to fast rise of temperature on a sub-picosecond time scale and the build-up of thermo-elastic stress followed by thermal expansion. This process results in the emission of coherent acoustic pulses with the shape resembling the initial energy deposition profile with a characteristic spatial scale δ_{heat} . The acoustic pulse duration is given by δ_{heat}/c_s , where $c_s = \sqrt{C_2/\rho}$ denotes the longitudinal speed of sound, ρ is material density and C_2 is determined by the elastic tensor and depends on the acoustic propagation direction [58].

The heat deposition depth δ_{heat} is determined not only by the optical skin depth, but also by the diffusion depth of laser-excited hot electrons during the thermalization time with initially cold lattice. This depth is given by $\delta_{\text{hot}} \sim \sqrt{\kappa/g}$, where κ and g denote the

thermal conductivity and electron-phonon coupling constant in the material, respectively [59]. In plasmonic metals characterized by relatively high thermal conductivity and weak electron-phonon coupling [60] the heat deposition depth $\delta_{\text{heat}} \simeq \delta_{\text{hot}} \sim 100$ nm largely exceeds the optical skin depth resulting in the generation of relatively long acoustic pulses with the duration of a few tens of picoseconds [61].

For noble metal films of thickness smaller than δ_{heat} , the temperature distribution is spatially homogeneous and the thermo-elastic dynamics can be reduced to breathing motion of the entire film consisting of the alternating expansion and contraction. This behaviour was evidenced in femtosecond time-resolved pump-probe experiments in Kretschmann configuration [62, 63, 64].

Hot electron diffusion in ferromagnetic metals appears to be less efficient ($\delta_{\text{hot}} \sim \delta_{\text{skin}} \sim 10$ nm) and results in the overall heat penetration depth $\delta_{\text{heat}} \sim 15\text{-}20$ nm [65, 66]. This short heat penetration depth in combination with a larger speed of sound suggests the generation of large-amplitude ultrashort acoustic pulses in ferromagnetic transition metals like Ni, Co and Fe. However, SPPs do not propagate on ferromagnet surfaces thereby rendering the plasmonic detection schemes extremely challenging. Up to now, there are no acousto-plasmonic investigations on thin ferromagnetic films.

The use of hybrid (noble metal)-ferromagnet bilayer structures on a dielectric substrate allows for the generation of ultrashort acoustic pulses in the ferromagnetic transducer and their plasmonic detection at the (noble metal)/air interface, see Fig. 9(a).

As the duration of the acoustic pulses is conserved upon the transmission from one elastic medium into another one, acoustic pulses

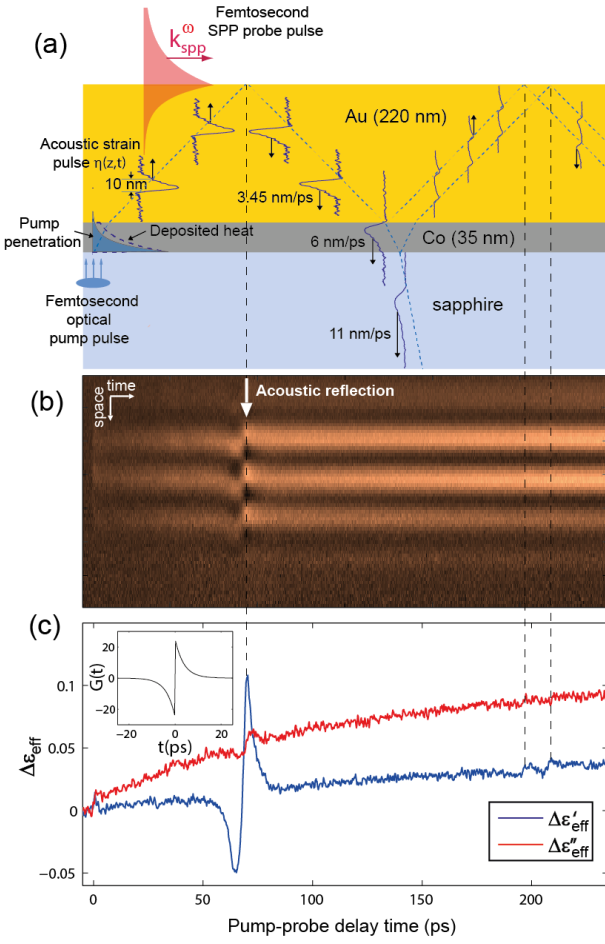


Figure 9. (a) In hybrid acousto-plasmonic structures the thermal expansion of cobalt transducer excited by a femtosecond pump pulse (fluence 7 mJ/cm²) at time zero launches an ultrashort acoustic pulse $\eta(z, t)$ propagating through (111) textured gold layer at the speed of sound $c_s = 3.45$ km/s. After approximately 70 ps, the acoustic reflection from gold-air interface changes the wave vector of a time-delayed ultrashort SPP probe pulse generating the acousto-plasmonic pump-probe interferogram (b) in a tilted slit-groove arrangement. The 10 nm wide acoustic strain pulse in (a) has a duration of 3 ps and is reconstructed from the dynamics of the time-dependent effective dielectric function $\Delta\epsilon_{\text{eff}}(t)$ in (c). The inset shows the acousto-plasmonic response function $G(t)$. Measurements are performed by time-resolved SPP interferometry [10, 66]

generated in cobalt are spatially compressed by a factor of 1.8 (ratio of sound velocities in cobalt and gold) down to 10 nm upon injection in softer gold [66].

Femtosecond time-resolved plasmonic interferometry [10] measures transient phase shifts of the plasmonic interferogram at the gold-air interface (Fig. 9(b)) caused by thermal and acoustic effects triggered by the absorption of an intense femtosecond pump pulse in cobalt layer. The reconstructed pump-induced modulation $\Delta\epsilon_{\text{eff}}(t) = \epsilon_{\text{eff}}(t) - \epsilon_{\text{Au}}$ in Fig. 9(c) displays the strong acoustic modulation capturing the reflection of the acoustic pulse $\eta(z, t)$ from the gold-air interface at 70 ps acoustic delay superimposed on a slowly varying thermal background (which will be neglected in the following discussion). The much weaker acousto-plasmonic signals observed at 197 ps and 208 ps are caused by the secondary 10% acoustic reflections from the gold-cobalt and cobalt-sapphire interfaces, respectively, and indicate a good acoustic impedance matching at these interfaces.

The quantitative reconstruction of the acoustic pulse $\eta(z, t)$ propagating in gold relies on the effective medium approximation. The compressional acoustic pulse in gold $\eta(z, t) = (n_i(z, t) - n_i^0)/n_i^0$ creates a layer of higher ion density $n_i(z, t) > n_i^0$, which moves at the sound velocity $c_s = 3.45$ nm/ps in gold in the (111) direction. Since the stationary charge separation between electrons and ions in a metal occurs only within the Thomas-Fermi radius $r_{\text{TF}} \sim 10^{-3}$ nm, the spatial profile of electron (charge) density $n_e(z, t)$ follows the ionic one: $n_e(z, t) = n_i(z, t)$. Evaluated at the probe photon energy of 1.55 eV, the dielectric function of gold, $\epsilon_{\text{Au}} = \epsilon' + i\epsilon'' = -24.8 + 1.5i$, is dominated by the free-carrier contribution with $\epsilon' \simeq -\omega_p^2/\omega^2 \propto -n_e$. An ultrashort acoustic strain pulse creates a time-dependent spatial profile of the dielectric function $\epsilon'(z, t) = \epsilon'[1 + \eta(z, t)]$ inside the metal, which modulates the SPP wave vector $k_{\text{spp}}(t) = k_0 \sqrt{\epsilon_{\text{eff}}(t)/(1 + \epsilon_{\text{eff}})}$, when the strain

pulse arrives within the SPP skin depth $\delta_{\text{skin}} = 13$ nm at the gold-air interface:

$$\varepsilon_{\text{eff}}(t) = \frac{\varepsilon_{\text{Au}}}{\delta_{\text{skin}}} \int_0^{\infty} [1 + \eta(z, t)] \exp(-z/\delta_{\text{skin}}) dz. \quad (14)$$

Using the explicit equation for the acoustic reflection at the (free) gold-air interface, $\eta(z, t) = \eta_0(t + z/c_s) - \eta_0(t - z/c_s)$, the integral over space can be converted into the integral over time. The real part of the acoustic modulation

$$\Delta\varepsilon'_{\text{eff}}(\tau) = \frac{|\varepsilon_{\text{Au}}|}{\tau_{\text{skin}}} \int_{-\infty}^{\infty} \eta_0(t) G(\tau - t) dt \quad (15)$$

of the effective dielectric function can be used to reconstruct the acoustic pulse $\eta_0(t)$. Here $\tau_{\text{skin}} = \delta_{\text{skin}}/c_s = 3.8$ ps denotes the acoustic travel time through the skin depth in gold (at 800 nm wavelength) and the acousto-plasmonic response function $G(t)$, defined as

$$G(t) = \exp(-|t|/\tau_{\text{skin}}) \text{sign}(t), \quad (16)$$

is shown in the inset in Fig. 9(c). Application of the Fourier-based algorithm [67] to $\Delta\varepsilon'_{\text{eff}}(\tau)$ allows to accurately reconstruct the acoustic pulse shape $\eta_0(t)$ with duration of 3 ps and spatial extent of 10 nm, as shown in Fig. 9(a). It is remarkable that plasmonic measurements provide the detailed shape of an acoustic pulse with the spatial dimensions smaller than the skin depth δ_{skin} .

Under certain conditions such shorter-than-skin-depth acoustic pulses can be also measured by simple time-resolved reflectivity measurements at the metal-dielectric interface, as shown for the gold-air interface at 400 nm optical probe wavelength [67].

4.2. Nonlinear acousto-plasmonics

The most striking advantage of the plasmonic interferometry as compared to the conventional pump-probe reflectivity analysis, is that it provides direct measurement of the absolute strain values. Upon increase of the peak

pump fluence up to 30 mJ/cm², the acoustic pulses reach very large amplitude of 1% and also change their shape, see Fig 10. The acoustic reshaping at high pump fluences becomes more pronounced in thicker gold films, which allowed us to establish its close relation to the acoustic propagation effects in gold [66]. The peak of the acoustic pulse, where the density of gold is higher, propagates through the gold layer at a higher speed of sound leading to the steepening of the acoustic pulse.

The results of the acousto-plasmonic measurements are found to be in an excellent quantitative agreement with the solutions of the non-linear Korteweg-de Vries (KdV) equation [68]

$$\frac{\partial \eta}{\partial t} + c_s \frac{\partial \eta}{\partial z} + \gamma \frac{\partial^3 \eta}{\partial z^3} + \frac{C_3}{2\rho c_s} \eta \frac{\partial \eta}{\partial z} = 0. \quad (17)$$

These dynamics are governed by the interplay between the acoustic broadening due to the phonon dispersion $\omega(q) = c_s q - \gamma q^3$ with $\gamma = 7.41 \times 10^{-18}$ m³/s and self-steepening and reshaping due to the elastic nonlinearity $C_3 = -2.63 \times 10^{12}$ kg/ms². See Ref. [58] for a definition of C_3 and Ref. [69, 70] for linear and higher order elastic constants in gold; $\rho = 19.2$ g/cm³ is the density of gold. The agreement between the nonlinear theory and the experiment is achieved by setting a single fit parameter, the initial heat penetration depth in cobalt to $\delta_{\text{heat}} = 20$ nm (corresponding to the initial pulse duration $\tau_0 = 3.2$ ps). This value is 50% larger than the optical skin depth in cobalt of 13 nm, indicating the importance of the electronic transport phenomena for establishing the initial distribution of thermal stress driving the thermo-elastic generation.

The quantitative agreement between theory and experiment for samples with different gold thickness demonstrated that nonlinear reshaping was dominated by acoustic nonlinear-

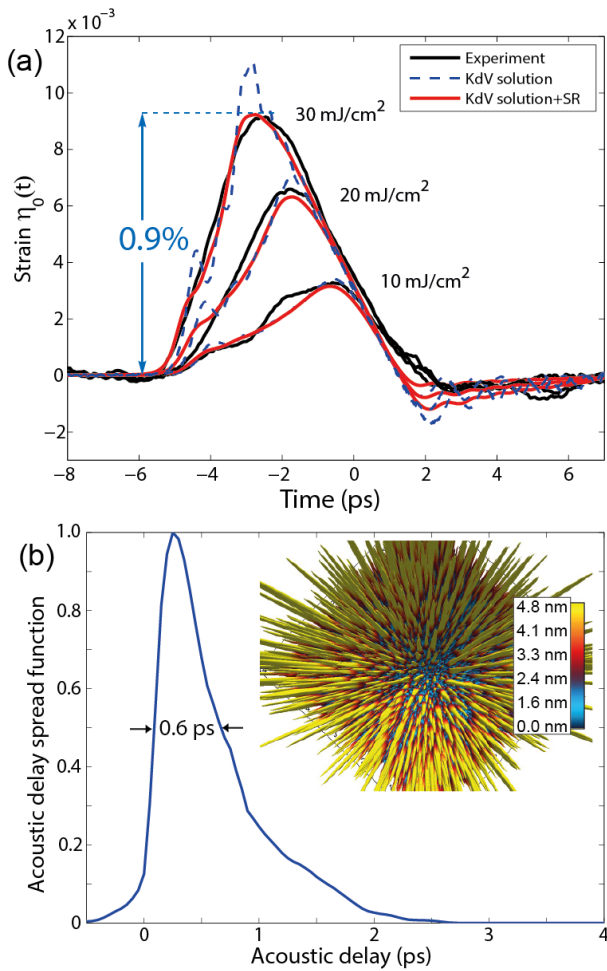


Figure 10. (a) The amplitude of acoustic pulses grows with the pump fluence, reaching nearly 1% whereas their shape changes. These shape changes are reversible and can be quantitatively described by the nonlinear acoustic propagation effects through a 220 nm thin gold layer. (b) Examination of the surface roughness (SR) by an atomic force microscopy (AFM) allows for the measurement of the topography of the gold-air interface. The nano-scale surface roughness (see the 3D-map of $5 \times 5 \mu\text{m}^2$ AFM scan in the inset) introduces substantial spread of the acoustic arrival times at the gold-air interface, quantified by the acoustic delay spread function. Figure (a) adopted with permission from ref. [66].

ities in gold, whereas a possible dependence of the initial strain shape in cobalt on pump power played a minor role [66]. The amplitude of the acoustic strain reached peak values $\eta_{\text{max}} \simeq 1\%$, corresponding to a compressional

stress $dp = c_s^2 \rho \eta_{\text{max}} = 2.3 \text{ GPa}$ before acoustic reflection and negative -2.3 GPa tensile stress afterwards. Control measurements at lower pump fluences confirmed that the nonlinear re-shaping presented in Fig. 10(a) was fully reversible. At even higher pump fluences in the range of 50 mJ/cm^2 , strain pulses with amplitudes reaching 1.5% were obtained. However, under such strong optical pumping consistent with elevating the lattice temperature in cobalt close to its melting point of 1768 K , irreversible degradation of the samples was observed.

Intrinsic damping of longitudinal phonons in gold caused by anharmonic phonon-phonon interactions [71] becomes increasingly important for frequencies exceeding 1 THz . However, in this frequency range and for our experimental geometry, the effect of nano-scale surface roughness entirely masks possible contributions due to phonon attenuation.

In order to illustrate this effect we have studied the topography of the gold-air interface at the position on the sample where acousto-plasmonic measurements were performed, by means of the atomic force microscopy (AFM). The inset in Fig. 10(b) shows a 3D representation of surface as seen by the acoustic pulses: given the tiny 3.45 nm wavelength of longitudinal acoustic phonons in (111) gold at 1 THz frequency, the nanoscale surface roughness results in the substantial distribution of acoustic arrival times at the gold-air interface. This effect is quantified in the histogram of the acoustic arrival times at the gold-air interface, which we denote as an acoustic delay spread function with a characteristic width of 0.6 ps . Therefore, all possible high-frequency components exceeding 1 THz forming ultrafast acoustic transients on a sub-picosecond time scale (such as, for example, acoustic solitons [58, 72, 73, 68]) are smeared out by the convolution with

the response function (compare KdV and KdV+SR curves in Fig. 10(a)).

The nonlinearity of acoustic propagation can be used to calibrate the conventional pump-probe reflectivity measurements, when the latter are compared with a quantitative experimental technique capable to measure the absolute values of strain amplitudes. Both ultrafast X-ray diffraction [74] and acousto-plasmonic interferometry [66] do a decent job. For example, the comparison of the KdV solutions with the fingerprints of the nonlinear acoustic reshaping observed in femtosecond pump-probe reflectivity measurements on the same structures [75] provides the values for photo-elastic coefficients $dn/d\eta = 2 \pm 0.7$ and $dk/d\eta = 1 \pm 0.3$ in gold at 400 nm probe wavelength, where $n + ik = 1.47 + 1.95i$ denotes the complex index of refraction. Accurately calibrated time-resolved reflectivity measurements carry the same physical information while offering considerable advantage over more complex quantitative techniques based on SPPs or X-rays.

When thinking in terms of the Kretschmann configuration, the nonlinearity of the acoustic propagation is unlikely to play a role due to the much smaller thickness, which typically does not exceed 50 nm for the entire multilayer structure. In contrast, the entire excitation about the nonlinear magneto-plasmonics is triggered by a much larger effect in the optical nonlinearities as compared to conventional plasmonics. It would be very instructive to learn if SHG intensity can be modulated by ultrashort acoustic pulses as well.

Here we illustrate a novel and poorly understood phenomenon of SHG modulation by acoustic pulses [76, 77, 78] with an example of femtosecond pump-probe measurements on a Au/Fe/Au/Fe multilayer structure grown epitaxially on a MgO(001) substrate. This

multilayer structure has been designed to study ultrafast transport of spin-polarized hot carriers in gold injected from laser-excited ferromagnetic iron discussed in Ref. [79].

In this study, we consider the influence of the acoustic pulses generated in the first 16 nm-thin iron layer on the SHG output in the second one, see Fig. 11. The elementary and oversimplified understanding of photo-acoustic generation suggests that femtosecond pump pulses are primarily absorbed in iron which then generates acoustic pulses propagating in both directions. A 3 nm-thin layer of gold aiming to protect the upper iron layer from oxidation acts as an acoustic delay line and results in the bi-polar acoustic pulse emitted into the thicker (49 nm) epitaxial Au(001) layer. An approximate pulse shape is shown in Fig. 11(a) for three distinct time moments τ_1, τ_2 and τ_3 corresponding to the arrival times of the sharp acoustic fronts at the second Fe/Au interface. This schematic helps to understand the effect of acoustic pulses on the linear reflectivity and SHG output from the second iron layer with the thickness $d_{Fe} = 15$ nm, see Fig. 11(b) and their high-resolution temporal zoom in Fig. 11(c). A few remarkable observations can be inferred from these measurements. First, the nonlinear acoustically-induced modulation $dI_{2\omega}/I_{2\omega}$ appears to be almost an order of magnitude larger as compared to the linear acoustic modulation $dR(t)/R$. Second, both optical signals are precisely correlated with the arrival times of acoustic fronts at the interfaces.

Interestingly, transient $dI_{2\omega}/I_{2\omega}$ (dSHG/SHG in Fig. 11) is a continuous function of time. A comparison of the SHG output variations with the linear reflectivity measurements in Fig. 11(c) clearly shows that the maximum compression (dilution) of the second iron layer

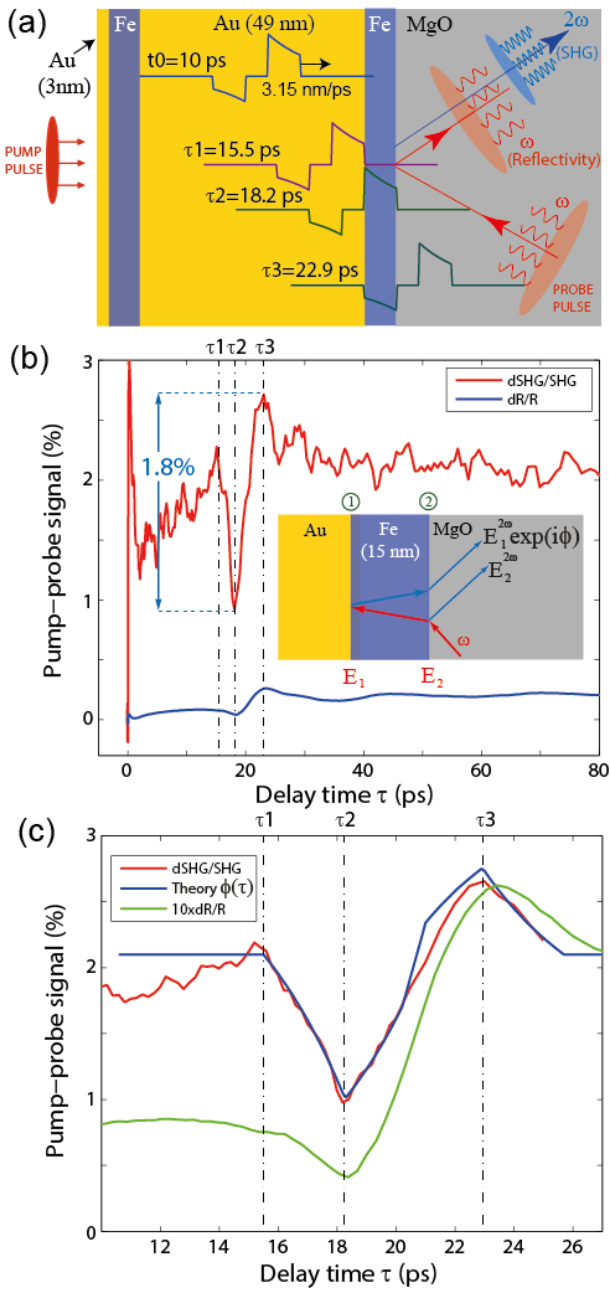


Figure 11. (a) Femtosecond optical pumping of an epitaxial (3 nm)Au/(16 nm)Fe/(49 nm)Au/(15 nm)Fe/MgO multilayer structure leads to the generation of a bipolar acoustic pulse propagating across the sample. (b) When passing through the second Fe layer, the acoustic pulse changes both linear reflectivity and SHG response to the ultrashort probe pulses. The inset shows a possible mechanism of SHG generation via two interfering contributions $E_1^{2\omega}$ and $E_2^{2\omega}$ from Au/Fe and Fe/MgO interfaces. (c) A high-resolution temporal scan shows a remarkable similarity in the dynamics of a strain-induced modulation of the optical phase $\phi(\tau)$ (see text for details).

correspond to the minimum (maximum) of both SHG intensity and reflectivity modulation. However, the fact that the kinks in the transient variations of the SHG signal are significantly narrower than those in linear reflectivity data demonstrates the extreme sharpness of the fronts of the acoustic pulses.

In centrosymmetric media SHG may arise due to electro-dipole (interface) or magneto-dipole and electro-quadrupole (bulk) contributions. It is commonly believed that the bulk contributions in metals are small as compared to the interface terms [35, 37, 80]. On the other hand, inversion symmetry in the bulk can be broken, for example, by a gradient of strain resulting in the allowed volumetric electro-dipole contribution. Whereas static strain gradients emerge from the growth on a lattice-mismatched substrate, dynamic strain gradients can be induced by ultrashort acoustic pulses. Another possible mechanism relies upon transient acoustic modulation of the surface properties of Fe, including the susceptibility tensor $\chi^{(2)}$. In any case, the total SHG output is produced by an interference of multiple SHG sources, whereas the interference conditions are strongly affected by the propagating acoustic pulses.

Despite these ambiguities, the shape of acoustically-induced SHG output modulation can be described within a simple model which considers an interference of the two surface SHG contributions $E_1^{2\omega} \exp(i\phi_0)$ and $E_2^{2\omega}$ generated at the Au/Fe and Fe/MgO interfaces. Here ϕ_0 denotes the phase difference between these two interfering terms suggesting that the total SHG intensity is proportional to $I_{2\omega} \propto |E_1^{2\omega} \exp(i\phi_0) + E_2^{2\omega}|^2$. An acoustic pulse $\eta(z, \tau)$ propagating through the iron layer modulates this optical phase

$\phi(\tau) = \phi_0 + \Delta\phi(\tau)$ according to

$$\Delta\phi(\tau) \propto \frac{2\pi}{\lambda} \int_0^{d_{\text{Fe}}} \eta(z, \tau) dz, \quad (18)$$

where the integration is performed over the entire Fe layer. As such, we obtain $dI_{2\omega} = -(2E_1^{2\omega} E_2^{2\omega} \sin \phi_0) \Delta\phi(\tau)$. Using the acoustic pulse shape shown in Fig. 11(a) and Eq. (18) we have calculated transient phase variations $\Delta\phi(\tau)$. With an appropriate scaling and vertical offset, this simulated phase shift demonstrates surprising similarity to the experimental SHG signal in Fig. 11(c). We note, however, that at present the underlying origin of this phase modulation remains unclear. Due to the nonlinear character of the discussed interference, this phase modulation is acquired by either the driving fundamental fields E_1 , E_2 or the emitted SHG field at the double frequency 2ω .

From a practical perspective, these preliminary experimental observations and theoretical modeling hold high potential in application to the nonlinear plasmonics and magneto-plasmonics. They can serve as a first step to test the effective interface approximation for complex multilayer structures, where a simple interference model can be generalized to include strain-induced modification of bulk SHG terms dominating in semiconductor and dielectric media [76, 78].

A more general phenomenological description using a single time-dependent nonlinear effective susceptibility $\chi_{\text{eff}}^{(2)}(t)$ for the upper interface in Fig. 7(b) would be also useful to understand the physical limits of ultrafast acoustic modulation in the nonlinear plasmonic switch sketched in Fig. 1.

5. Fabrication and characterization of multilayer structures

The quality of the samples determines the effects which can be experimentally observed. For instance, for the plasmonic experiments, the key optimization of the samples consists in the minimization of the sample roughness [81]. In stark contrast, ultrafast acoustics turns out to be much more demanding to the sample quality with many parameters drastically influencing the observed signal amplitudes and shapes of the transients. Those parameters include the surface and interface roughness, single- or polycrystallinity of the samples, grain sizes and grain size distribution as well as the texture of the grains. For the latter, due to the large elastic anisotropy of crystalline solids, the acoustic propagation time in grains with different orientation would typically differ by 10% around the average value: The commonly used value of 3200 m/s for polycrystalline gold differs from 3450 m/s for (111) and 3150 m/s for (100) crystallographic directions in gold single crystals.

For the experiments on ultrafast acoustics discussed in this review, the most appropriate substrates are $\text{Al}_2\text{O}_3(0001)$. Due to their single crystal nature, they assure excellent optical transparency in the relevant frequency range and offer good acoustic impedance matching to cobalt. The latter is a good transducer for ultrafast acoustics because of its high speed of sound and high melting temperature. Since the details of the layer stack are already defined for the efficient magneto-acousto-plasmonics, the remaining optimization of the sample quality is mainly related to the adjustment of the growth parameters of the Co layer and Au films, with the target to improve homogeneity of the respective materials.

One of the key parameters determining

the crystalline structure of Co when grown on $\text{Al}_2\text{O}_3(0001)$ is the deposition temperature. This temperature should be chosen to obtain strong hcp (0001) texture of Co thin films which should promote the growth of the (111) textured Au layer. A rather large lattice mismatch of about 14% between fcc Au(111) and hcp Co(0001) is relieved by formation of misfit dislocations [82], which assures the emergence of laterally extended grains of (111) textured Au on top of the Co film. We note that the deposition at temperatures of lower than 200°C does not result in a clear texture of Co films on $\text{Al}_2\text{O}_3(0001)$ even when rather thick (80 nm) films are deposited [83]. At the same time, growth at temperatures of above 400°C might favor the Co layer to arrange in fcc rather than hcp structure, because according to the equilibrium phase diagram of Co, the hcp to fcc transformation temperature is 422°C . In the temperature window between 200°C and 400°C , the substrate temperature is sufficiently large to result in a Co film with hexagonal crystal structure and a full epitaxial relation $\text{Co}(0001) \langle 10 - 10 \rangle \parallel \text{Al}_2\text{O}_3(0001) \langle 11 - 20 \rangle$. Although films grown at higher temperatures typically possess larger grain sizes, deposition of Au on top of Co at 400°C might result in the intermixing at the interface. In accordance with Ref.[84, 85], annealing in H_2/N_2 atmosphere at temperatures up to 300°C allows to avoid alloying. However, vacuum annealing of Co/Au multilayers up to 250°C leads to the partial loss of the structural coherence which might be indicative for the Co-Au mixture formation [86]. Based on these considerations, the appropriate temperature window for the sample growth is between 200 and 250°C .

The deposition of Co and Au thin films is carried out at 250°C using dc-magnetron sputtering in a high vacuum chamber with

a base pressure of 10^{-7} mbar. Double-side epipolished $500 \mu\text{m}$ -thick $\text{Al}_2\text{O}_3(0001)$ single crystals (Crystec GmbH) with lateral dimensions of $10 \times 10 \text{ mm}^2$ were used as a substrate. The tilt of the c-axis of the $\text{Al}_2\text{O}_3(0001)$ was less than 0.3° . The substrates were fixed to the sample holder using metal clamps assuring good thermal contact. Before the deposition, the substrates were outgassed for 30 min at 250°C . Ar was used as a sputter gas (Ar pressure is 3.5×10^{-3} mbar). The deposition rate of Co and Au was set to 0.2 \AA/s and 2 \AA/s , respectively. The thickness of Co layer was varied between 2 and 35 nm. The thickness of Au film was chosen between 120 and 780 nm.

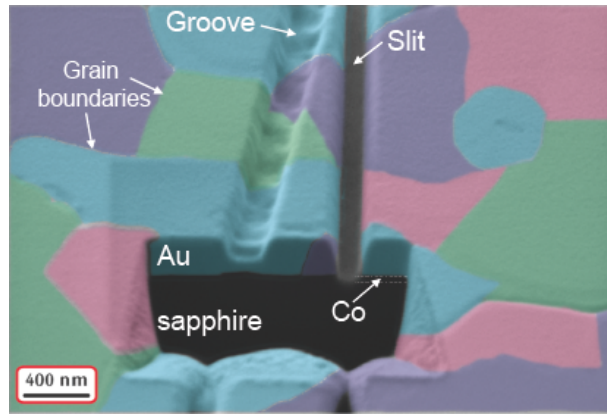


Figure 12. All investigated gold films grown by magnetron sputtering at 250°C displayed (111) texture and a large grain size of the order of $1 \mu\text{m}$. Small changes in the SEM images from secondary electrons were color-coded to show different grains.

The structural analysis of the samples with Co(2 nm; 4 nm; 6 nm) / Au(200 nm) has been performed by X-ray diffraction (XRD) in Bragg-Brentano geometry using Cu K_α irradiation (wavelength: 1.54 \AA) on a laboratory diffractometer (XRD 7, Seifert-FPM). Due to the small thickness, the diffraction peaks of Co are not resolved. Independent of the thickness of Co, a clear diffraction peak at 38.35° is observed

characteristic of (111) textured Au films. Although the films are strongly (111) textured, the in-plane orientation of the Au crystallites is random, as can be seen when analyzing the scanning electron microscopy (SEM) image (Fig. 12). Different in-plane orientation of the crystallites is shown using false colors. The size of an individual crystallite is in the range of few hundreds of nanometers. Furthermore, the cross-section of the film was studied by cutting it using focused-ion beam etching. We conclude that each grain is uniform in thickness due to the excellent homogeneity in the SEM contrast. This finding has a strong implication for the analysis of the propagation of acoustic pulses in the film: as the gold film is (111) textured, the propagation velocity of an acoustic pulse along the film thickness can be taken as constant and equal to the 3450 m/s, the characteristic value for the a single crystal with (111) orientation.

6. Discussion and future research

In this study we did not discuss any investigations related to the ultrafast magnetization dynamics [87]. The phenomenon of ultrafast laser-induced demagnetization, either by the direct optical excitation [52] or mediated by the ultrafast transport of non-equilibrium hot electrons across the (noble metal)-ferromagnet interface [79, 88, 54, 89, 55], results in the abrupt decrease in the length of magnetization vector. This phenomenon occurs on a sub-picosecond time scale and can even result in ultrafast magnetization reversal in ferrimagnets [90, 91].

Another option of the laser-induced magnetization control consists in changing the direction of magnetization as evidenced by the excitation of the ferromagnetic resonance (FMR) precession. FMR precession [92, 53, 93]

as well as excitation of spatially inhomogeneous (magnon) precessional modes in ferromagnetic thin films [53, 55] originate from the ultrafast thermally-induced changes in the magneto-crystalline anisotropy.

Very recently, it became typical to induce FMR precession via magneto-elastic interactions in ferromagnets, when excited by picosecond acoustic strain pulses [94, 95, 96]. So far the acoustically induced FMR precession in thin ferromagnetic films was observed only when the symmetry was broken by the non-zero out-of-plane component of the external magnetic field [94, 95, 96]. In the analogous experiments with ultrafast surface acoustic waves (SAW, excited by fs-laser pulses in transient grating geometry [97]), the most efficient excitation of FMR precession was achieved by tilting the external magnetic field with respect to the SAW wave vector [98, 99]. Further, a laser excitation of a coupled magneto-elastic mode with an extreme lifetime of more than 25 ns and strongly nonlinear behaviour was demonstrated in ferromagnetic dielectric FeBO₃ [100].

Purely acoustic magnetization switching was predicted theoretically for single-crystal thin film of magnetostrictive metal Terfenol-D excited with picosecond acoustic pulses [101] or semiconductor (Ga,Mn)(As,P) driven by quasi-monochromatic SAW transients [102]. Experimentally, acoustic magnetization switching has only been demonstrated in ferromagnetic nanoparticles on the nanosecond time scale [103]. From all these observations we conclude that in the nonlinear plasmonic switch sketched in Fig. 1, notably with an in-plane magnetic field applied, the magneto-acoustic effects are unlikely to play a major role.

The substantial modulation of the nonlinear optical properties of 1.8% can be further

enhanced by functionalizing the structure with a monolayer of semiconductor quantum dots (QDs). QDs are particularly promising for nonlinear acousto-magneto-plasmonics as they feature configurable "atom-like" optical excitation spectrum because they offer the ability of engineering of the electron and hole wave functions via the QD size R_{QD} . Nonlinear initialization and readout of singly-charged QDs can be harvested for ultrafast quantum optical functionality [104]. It is known that a linear as well as a nonlinear response in these systems, typically analyzed in the dipole approximation which exploits the approximation $R_{\text{QD}} \ll \lambda$, is intimately linked to the details of the spin configuration of the few-electron states as well as the crystal structure and the geometry of the nano-emitter [105, 106]. Application of controlled acoustic transients with considerable enhancement in the elastic field gradients on the length scales comparable to R_{QD} would thus allow for controlled studies of the response of the quantum system beyond the dipole approximation [107]. In other words, if the acoustic pulse can significantly perturb the electron eigenstates in the quantum dot, new fascinating electromagnetic effects of substantially non-local nature can be expected. This nonlinear coupled regime has not been well explored so far and might provide new physical insights and therefore inspire novel photonic applications. As a parting example we speculate that by subjecting colloidal quantum dots [108] to intense acoustic transients such as those reviewed here, one might be able to drive structural phase transition [109] in these crystal on ultrafast timescales. As a result, one would be able to directly switch and control the brightness of the quantum emitter [105] on femtosecond time scales.

Beyond the SHG response, higher nonlinearities such as third-order susceptibility-

driven magnetic third harmonic generation (mTHG) can be exploited to great effect. Indeed, mTHG allows to evaluate bulk (as compared to surface mSHG) nonlinearities and also draw analogies to the giant magnetoresistance properties in ferromagnetic nanostructures [110]. In our case, for the THG frequency to fall in the visible spectral range, one would need to apply pump excitation with a wavelength in the near-infrared spectral range [111, 112]. Employing the telecom wavelengths ($\lambda = 1.3$ or $1.5 \mu\text{m}$) would allow to simultaneously detect mSHG and mTHG in the visible spectral range, while exploiting mature technology of ultrabroadband femtosecond fiber lasers [113]. Moreover, in this case SPP excitation at the first and the second harmonic frequencies will occur at nearly the same angle and as a result would lead to a more favorable phase-matching condition between the SPPs, $k_{\text{spp}}^{2\omega} \simeq 2k_{\text{spp}}^{\omega}$. Moving to even longer wavelengths and using intense pulses of THz radiation as an effective stimulus may enable efficient high-order harmonic generation with SPPs.

To summarize, in this paper we have discussed some recent developments in the field of the nonlinear acousto-magneto-plasmonics, which are necessary for understanding of the fundamental interactions and the associated time and length scales of the nonlinear plasmonic switch sketched in Fig. 1. The extension of the concepts presented here to hybrid plasmonic structures as well as to semiconductor nanostructures, together with shifting the experimental focus to lower photon energies and higher-order optical nonlinearities hold high potential for future research.

6.1. Acknowledgments

Authors thank A. Alekhin (FHI Berlin) for performing the nonlinear SHG-measurements shown in Fig. 11 and T. Thomay (SUNY at Buffalo) for focussed ion beam milling of the plasmonic microinterferometers and taking a false-color SEM image of Au/Co/sapphire structure in Fig. 12. They also acknowledge stimulating discussions with U. Woggon, A. Leitenstorfer, A. Kirilyuk, Th. Rasing, T.V. Murzina, R. Bratschitsch, R. Tobey, A. Garcia-Martin, V.S. Vlasov, A.M. Lomonosov, V. Juvé, P. Ruello, V.E. Gusev, I. Radu, U. Bovensiepen, T. Kampfrath, M. Bargheer, P. Gaal and M. Wolf.

Funding from *Nouvelle équipe, nouvelle thématique* "Ultrafast acoustics in hybrid magnetic nanostructures" and *Stratégie internationale* "NNN-Telecom" de la Région Pays de La Loire, DFG (TE770/1), ANR-DFG "PPMI-NANO" (ANR-15-CE24-0032 & DFG SE2443/2), ANR "UltramoX" (ANR-14-CE26-0008), U.S. DOE Grant no. DE-FG02-00ER15087, U.S. NSF Grant no. CHE-1111557, the European Research Council (FP7/2007-2013) / ERC grant agreement no. 306277 and *Alexander von Humboldt Stiftung* is highly appreciated.

7. References

- [1] Y. Fedutik, V. V. Temnov, O. Schöps, U. Woggon, and M. V. Artemyev. Exciton-plasmon-photon conversion in plasmonic nanostructures. *Phys. Rev. Lett.*, 99:136802, 2007.
- [2] A. Ueda, T. Tayagaki, and Y. Kanemitsu. Energy transfer from semiconductor nanocrystal monolayers to metals surfaces revealed by time-resolved photoluminescence spectroscopy. *Appl. Phys. Lett.*, 92:133118, 2008.
- [3] M. Pelton, J. Aizpurua, and G. Bryant. Metal-nanoparticle plasmonics. *Laser and Photon. Rev.*, 2:136–159, 2008.
- [4] K. Wang and D. M. Mittleman. Dispersion of surface plasmon polaritons on metal wires in the terahertz frequency range. *Phys. Rev. Lett.*, 96:157401, 2006.
- [5] E. Kretschmann and H. Raether. Radiative decay of non radiative surface plasmons excited by light. *Z. Naturforsch.*, 23a:2135–2136, 1968.
- [6] J.J. Burke, G.I. Stegeman, and T. Tamir. Surface-polariton-like waves guided by thin, lossy metal films. *Phys. Rev. B*, 33:5186, 1986.
- [7] W. H. Weber and G. W. Ford. Optical electric-field enhancement at a metal surface arising from surface-plasmon excitation. *Opt. Lett.*, 6:122, 1981.
- [8] Jacob B. Khurgin. How to deal with the loss in plasmonics and metamaterials. *Nature Nanotechnology*, 10:2–6, 2015.
- [9] P. Nagpal, N.C. Lindquist, S.H. Oh, and D.J. Norris. Ultrasmooth patterned metals for plasmonics and metamaterials. *Science*, 325:594–597, 2009.
- [10] V. V. Temnov, K. Nelson, G. Armelles, A. Cebollada, T. Thomay, A. Leitenstorfer, and R. Bratschitsch. Femtosecond surface plasmon interferometry. *Opt. Express*, 17:8423–8432, 2009.
- [11] A.V. Zayats, I.I. Smolyaninov, and A.A. Maradudin. Nano-optics of surface plasmon polaritons. *Physics Reports*, 408:131–314, 2005.
- [12] G. Gay, O. Alloschery, B. Viaris de Lesegno, C. O'Dwyer, J. Weiner, and H. J. Lezec. The response of nanostructured surfaces in the near field. *Nature Phys.*, 2:262, 2006.
- [13] V. V. Temnov, U. Woggon, J. Dintinger, E. Devaux, and T. W. Ebbesen. Surface plasmon interferometry: measuring group velocity of surface plasmons. *Opt. Lett.*, 32:1235, 2007.
- [14] D. Pacifici, H. J. Lezec, and H. A. Atwater. All-optical modulation by plasmonic excitation of cdse quantum dots. *Nature Phot.*, 1:402–406, 2007.
- [15] G. Armelles, A. Cebollada, A. Garcia-Martin, and M. U. Gonzalez. Magnetoplasmonics: Combining magnetic and plasmonic functionalities. *Adv. Opt. Mater.*, 1:10–35, 2013.
- [16] G. Ctistis, E. Papaioannou, P. Patoka, J. Gutek, P. Fumagalli, and M. Giersig. Optical and magnetic properties of hexagonal arrays of subwavelength holes in optically thin cobalt

- films. *Nano Lett.*, 9(1):1–6, 2009.
- [17] Y. Demidenko, D. Makarov, O.G. Schmidt, and V. Lozovski. Surface plasmon-induced enhancement of the magneto-optical kerr effect in magnetoplasmonic heterostructures. *J. Opt. Soc. Am. B*, 28:2115, 2011.
- [18] V. Bonanni, S. Bonetti, T. Pakizeh, Z. Pirzadeh, J. Chen, J. Nogues, P. Vavassori, R. Hillenbrand, J. Åkerman, and A. Dmitriev. Designer magnetoplasmonics with nickel nanoferrimagnets. *Nano Lett.*, 11:5333–5338, 2011.
- [19] V. I. Belotelov, L. E. Kreilkamp, I. A. Akimov, A. N. Kalish, D. A. Bykov, S. Kasture, V. J. Yallapragada, Achanta Venu Gopal, A. M. Grishin, S. I. Khartsev, M. Nur-E-Alam, M. Vasiliev L. L. Doskolovich D. R. Yakovlev, K. Alameh, A. K. Zvezdin, and M. Bayer. Plasmon-mediated magneto-optical transparency. *Nat. Commun.*, 4:2128, 2013.
- [20] I. Crassee, M. Orlita, M. Potemski, A. L. Walter, M. Ostler, Th. Seyller, I. Gaponenko, J. Chen, and A. B. Kuzmenko. Intrinsic terahertz plasmons and magnetoplasmons in large scale monolayer graphene. *Nano Lett.*, 12:2470–2474, 2012.
- [21] N. Maccaferri, A. Berger, S. Bonetti, V. Bonanni, M. Kataja, Q. H. Qin, S. van Dijken, Z. Pirzadeh, A. Dmitriev, J. Nogues, J. Åkerman, and P. Vavassori. Tuning the magneto-optical response of nanosize ferromagnetic ni disks using the phase of localized plasmons. *Phys. Rev. Lett.*, 111:167401, 2013.
- [22] M. R. Shcherbakov, P. P. Vabishchevich and A. Yu. Frolov, T. V. Dolgova, and A. A. Fedyanin. Femtosecond intrapulse evolution of the magneto-optic kerr effect in magnetoplasmonic crystals. *Phys. Rev. B*, 90:201405(R), 2014.
- [23] M. Autore, H. Engelkamp, F. DApuzzo, A. Di Gaspare, P. Di Pietro, I. Lo Vecchio, M. Brahlek, N. Koirala, S. Oh, and S. Lupi. Observation of magnetoplasmons in bi2se3 topological insulator. *ACS Photonics*, 2:1231–1235, 2012.
- [24] N. Maccaferri, K. E. Gregorczyk, T. V. A. G. de Oliveira, M. Kataja, S. van Dijken, Z. Pirzadeh, A. Dmitriev, J. Åkerman, M. Knez, and P. Vavassori. Ultrasensitive and label-free molecular-level detection enabled by light phase control in magnetoplasmonic nanoantennas. *Nat. Commun.*, 6:6150, 2015.
- [25] I. S. Maksimov. Magneto-plasmonics and resonant interaction of light with dynamic magnetisation in metallic and all-magneto-dielectric nanostructures. *Nanomaterials*, 5:577–613, 2015.
- [26] V. V. Temnov, G. Armelles, U. Woggon, D. Guzatov, A. Cebollada, A. Garcia-Martin, J. M. Garcia-Martin, T. Thomay, A. Leitenstorfer, and R. Bratschitsch. Active magnetoplasmonics in hybrid metal-ferromagnet structures. *Nature Photon.*, 4:107–110, 2010.
- [27] I. Razdolski, D. Makarov, O.G. Schmidt, A. Kirilyuk, Th. Rasing, and V.V. Temnov. Nonlinear surface magnetoplasmonics in Kretschmann multilayers. *ACS Photonics*.
- [28] V. V. Temnov. Ultrafast acousto-magneto-plasmonics. *Nature Photon.*, 6:728–736, 2012.
- [29] J. F. Torrado, J. B. Gonzalez-Diaz, A. Garcia-Martin, and G. Armelles. Unraveling the relationship between electromagnetic field intensity and the magnetic modulation of the wave vector of coupled surface plasmon polaritons. *New J. Phys.*, 15:075025, 2013.
- [30] V.I. Belotelov, D.A. Bykov, L.L. Doskolovich, A.N. Kalish, and A.K. Zvezdin. Extraordinary transmission and giant magneto-optical transverse kerr effect in plasmonic nanostructured films. *J. Opt. Soc. Am. B*, 26:1594–1598, 2009.
- [31] J. J. Foley IV, H. Harutyunyan, D. Rosenmann, R. Divan, G. P. Wiederrecht, and S. K. Gray. When are surface plasmon polaritons excited in the kretschmann-raether configuration? *Sci. Rep.*, 5:9929, 2015.
- [32] K. F. MacDonald, Z. L. Samson, M. I. Stockman, and N. I. Zheludev. Ultrafast active plasmonics. *Nature Photon.*, 3:55–58, 2008.
- [33] M. Kauranen and A. V. Zayats. Nonlinear plasmonics. *Nat. Photon.*, 6:737–748, 2012.
- [34] W. Zheng, X. Liu, A.T. Hanbicki, B.T. Jonker, and G. Lüpke. Nonlinear magneto-plasmonics. *Opt. Mater. Expr.*, 5:2597–2607, 2015.
- [35] M. B. Raschke, S. Berweger, and J.M. Atkin. Ultrafast and nonlinear plasmon dynamics. In T.V. Shahbazyan and M.I. Stockman, editors, *Plasmonics: Theory and Applications*, pages 237–281. Springer, Berlin, 2013.
- [36] H. J. Simon, D. E. Mitchell, and J. G. Watson. Optical second-harmonic generation with surface plasmons in silver films. *Phys.*

- Rev. Lett.*, 33:1531–1534, 1974.
- [37] T. F. Heinz. *Second-order nonlinear optical effects at surfaces and interfaces*, chapter 5, pages 353–416. Elsevier, Amsterdam, 1991.
- [38] F. de Martini and Y. R. Shen. Nonlinear excitation of surface polaritons. *Phys. Rev. Lett.*, 36:216–219, 1976.
- [39] S. Palomba and L. Novotny. Nonlinear excitation of surface plasmon polaritons by four-wave mixing. *Phys. Rev. Lett.*, 101:056802, 2008.
- [40] Ru-Pin Pan, H. D. Wei, and Y. R. Shen. Optical second-harmonic generation from magnetized surfaces. *Phys. Rev. B*, 39(2):1229–1234, 1989.
- [41] V.L. Krutyanskiy, I.A. Kolmychek, E.A. Ganshina, T.V. Murzina, P. Evans, R. Pollard, A.A. Stashkevich, G.A. Wurtz, and A.V. Zayats. Plasmonic enhancement of nonlinear magneto-optical response in nickel nanorod metamaterials. *Phys. Rev. B*, 87:035116, 2013.
- [42] I. Razdolski, D. G. Gheorghe, E. Melander, B. Hjörvarsson, P. Patoka, A. V. Kimel, A. Kirilyuk, E. Th. Papaioannou, and Th. Rasing. Nonlocal nonlinear magneto-optical response of a magnetoplasmonic crystal. *Phys. Rev. B*, 88:075436, 2013.
- [43] V. L. Krutyanskiy, A. L. Chekhov, V. A. Ketsko, A. I. Stognij, and T. V. Murzina. Giant nonlinear magneto-optical response of magnetoplasmonic crystals. *Phys. Rev. B*, 91:121411(R), 2015.
- [44] T.V. Murzina, T.V. Misuryaev, A.F. Kravets, J. Guedde, D. Schuhmacher, G. Marowsky, A.A. Nikulin, and O.A. Aktsipetrov. Nonlinear magneto-optical kerr effect and plasmon-assisted shg in magnetic nanomaterials exhibiting giant magnetoresistance. *Surf. Sci.*, 482–485:1101–1106, 2001.
- [45] O.A. Aktsipetrov, T.V. Murzina, E.M. Kim, R.V. Kapra, A.A. Fedyanin, M. Inoue, A.F. Kravets, S.V. Kuznetsova, M.V. Ivanchenko, and V.G. Lifshits. Magnetization-induced second- and third-harmonic generation in magnetic thin films and nanoparticles. *J. Opt. Soc. Am. B*, 22(1):138–147, 2005.
- [46] I. A. Kolmychek, T. V. Murzina, S. Fourier, J. Wouters, V. K. Valev, T. Verbiest, and O. A. Aktsipetrov. Second harmonic generation in core (shell) γ - Fe_2O_3 (au) nanoparticles. *Sol. State Phenom.*, 152–153:508–511, 2009.
- [47] Ventsislav K. Valev, Alejandro V. Silhanek, Werner Gillijns, Yogesh Jeyaram, Hanna Padubrouskaya, Alexander Volodin, Claudiu G. Biris, Nicolae C. Panoiu, Ben De Clercq, Marcel Ameloot, Oleg A. Aktsipetrov, Victor V. Moshchalkov, , and Thierry Verbiest. Plasmons reveal the direction of magnetization in nickel nanostructures. *ACS Nano*, 5(1):91–96, 2011.
- [48] W. Zheng, A. Hanbicki, B. T. Jonker, and G. Lüpke. Control of magnetic contrast with nonlinear magneto-plasmonics. *Sci. Rep.*, 4:1–5, 2014.
- [49] Nicolai B. Grosse, Jan Heckmann, and Ulrike Woggon. Nonlinear plasmon-photon interaction resolved by k-space spectroscopy. *Phys. Rev. Lett.*, 108(13):136802, 2012.
- [50] J. Heckmann, M.-E. Kleemann, N. B. Grosse, and U. Woggon. The dual annihilation of a surface plasmon and a photon by virtue of a three-wave mixing interaction. *Opt. Express*, 21:28856–28861, 2013.
- [51] V. V. Pavlov, G. Tessier, C. Malouin, P. Georges, A. Brun, D. Renard, P. Meyer, J. Ferre, and P. Beauvillain. Observation of magneto-optical second-harmonic generation with surface plasmon excitation in ultrathin au/co/au films. *Appl. Phys. Lett.*, 75(2):190–192, 1999.
- [52] E. Beaupaire, J. C. Merle, A. Daunois, and J.-Y. Bigot. Ultrafast spin dynamics in ferromagnetic nickel. *Phys. Rev. Lett.*, 76:4250–4253, 1996.
- [53] M. van Kampen, C. Jozsa, J. T. Kohlhepp, P. LeClair, L. Lagae, W. J. M. de Longe, and B. Koopmans. All-optical probing of coherent spin waves. *Phys. Rev. Lett.*, 88(227201), 2002.
- [54] A. Eschenlohr, M. Battiato, P. Maldonado, N. Pontius, T. Kachel, K. Holldack, R. Mitzner, A. Fohlisch, P. M. Oppeneer, and C. Stamm. Ultrafast spin transport as key to femtosecond demagnetization. *Nature Mat.*, 12:332336, 2013.
- [55] V. Shalagatskyi, O. Kovalenko, V. Shumylo, T. Pezeril, D. Mounier, V. E. Gusev, D. Makarov, and V. V. Temnov. Ultrafast electron-phonon-magnon interactions at noble metal-ferromagnet interfaces. *arXiv:1511.09060*, 2015.
- [56] C. Thomsen, H. T. Grahn, H. J. Maris, and J. Tauc. Surface generation and detection of phonons by picosecond light pulses. *Phys. Rev.*

- B*, 34:4129–4138, 1986.
- [57] O. Matsuda, M.C. Larciprete, R.L. Voti, and O.B. Wright. Fundamentals of picosecond laser ultrasonics. *Ultrasonics*, 56:3–20, 2015.
- [58] H. Y. Hao and H. J. Maris. Experiments with acoustic solitons in crystalline solids. *Phys. Rev. B*, 64:064302, 2001.
- [59] G. Tas and H. J. Maris. Electron diffusion in metals studied by picosecond ultrasonics. *Phys. Rev. B*, 49:15046, 1994.
- [60] N. Del Fatti, C. Voisin, M. Achermann, S. Tzortzakis, D. Christofilos, and F. Vallée. Nonequilibrium electron dynamics in noble metals. *Phys. Rev. B*, 61:16956–16966, 2000.
- [61] V.E. Gusev and O.B. Wright. Ultrafast nonequilibrium dynamics of electrons in metals. *Phys. Rev. B*, 57:2878, 1998.
- [62] M. van Exter and A. Legendijk. Ultrashort surface-plasmon and phonon dynamics. *Phys. Rev. Lett.*, 60:49–52, 1988.
- [63] J. Wang, J. Wu, and C. Guo. Resolving dynamics of acoustic phonons by surface plasmons. *Opt. Lett.*, 32:719–721, 2007.
- [64] J. Wang and C. Guo. Effect of electron heating on femtosecond laser-induced coherent acoustic phonons in noble metals. *Phys. Rev. B*, 75:184304, 2007.
- [65] T. Saito, O. Matsuda, and O. B. Wright. Picosecond acoustic phonon pulse generation in nickel and chromium. *Phys. Rev. B*, 67:205421, 2003.
- [66] V. V. Temnov, C. Klieber, K. A. Nelson, T. Thomay, V. Knittel, A. Leitenstorfer, D. Makarov, M. Albrecht, and R. Bratschitsch. Femtosecond nonlinear ultrasonics in gold probed with ultrashort surface plasmons. *Nature Communications*, 4:1468, 2013.
- [67] K.J. Manke, A.A. Maznev, C. Klieber, V. Shalagatskyi, V.V. Temnov, D. Makarov, S.-H. Baek, C.-B. Eom, and K.A. Nelson. Measurement of shorter-than-skin-depth acoustic pulses in a metal film via transient reflectivity. *Appl. Phys. Lett.*, 103:173104, 2013.
- [68] P.J.S. van Capel, E. Péronne, and J.I. Dijkhuis. Nonlinear ultrafast acoustics at the nano scale. *Ultrasonics*, 56:36–51, 2015.
- [69] J. Behari and B.B. Tripathi. Phonon dispersion in noble metals. *J. Phys. C: Sol. St. Phys.*, 3:659–664, 1970.
- [70] Y. Hiki and A.V. Granato. Anharmonicity in noble metals; higher order elastic constants. *Phys. Rev.*, 144:411–419, 1966.
- [71] X. Tang and B. Fultz. First-principles study of phonon linewidths in noble metals. *Phys. Rev. B*, 84:054303, 2011.
- [72] P. J. S. van Capel and J. I. Dijkhuis. Time-resolved interferometric detection of ultrafast strain solitons in sapphire. *Phys. Rev. B*, 81:144106, 2010.
- [73] H.J. Maris and S. Tamura. Propagation of acoustic phonon solitons in nonmetallic crystals. *Phys. Rev. B*, 84:024301, 2011.
- [74] A. Bojahr, M. Herzog, D. Schick, I. Vrejoiu, and M. Bargheer. Calibrated real-time detection of nonlinearly propagating strain waves. *Phys. Rev. B*, 86:144306, 2012.
- [75] T. Pezeril, C. Klieber, V. Shalagatskyi, G. Vaudel, V.V. Temnov, O.G. Schmidt, and D. Makarov. Femtosecond imaging of nonlinear acoustics in gold. *Opt. Express*, 22:4590–4598, 2014.
- [76] H.B. Zhao, Y. Fan, G. Lüpke, A.T. Hanbicki, C.H. Li, and B.T. Jonker. Detection of coherent acoustic phonons by time-resolved second-harmonic generation. *Phys. Rev. B*, 83:2012302, 2011.
- [77] A.Y. Bykov, T.V. Murzina, N. Olivier, G.A. Wurtz, and A.V. Zayats. Coherent lattice dynamics in topological insulator Bi_2Te_3 probed with time-resolved optical second-harmonic generation. *Phys. Rev. B*, 92:064305, 2015.
- [78] L. Huber, A. Ferrer, T. Kubacka, T. Huber, C. Dornes, T. Sato, K. Ogawa, K. Tono, T. Katayama, Y. Inubushi, M. Yabashi, Y. Tanaka, P. Beaud, M. Fiebig, V. Scagnoli, U. Staub, and S. L. Johnson. Coherent acoustic perturbation of second-harmonic generation in nio. *Phys. Rev. B*, 92:094304, 2015.
- [79] A. Melnikov, I. Razdolski, T.O. Wehling, E.Th. Papaioannou, V. Roddatis, P. Fumagalli, O. Aktsipetrov, A.I. Lichtenstein, and U. Bovensiepen. Ultrafast transport of laser-excited spin-polarized carriers in $\text{Au/Fe/MgO}(001)$. *Phys. Rev. Lett.*, 107:076601, 2011.
- [80] Fu Xiang Wang, Francisco J. Rodriguez, Willem M. Albers, Risto Ahorinta, J. E. Sipe, and Martti Kauranen. Surface and bulk contributions to the second-order nonlinear optical response of a gold film. *Phys. Rev. B*, 80:233402, 2009.
- [81] K.M. McPeak, S.V. Jayanti, S.J.P. Kress,

- S. Meyer, S. Iotti, A. Rossinelli, and D.J. Norris*. Plasmonic films can easily be better: Rules and recipes. *ACS Photonics*, 2015.
- [82] C.H. Lee, H. He, F. Lamelas, W. Vavra, C. Uher, and R. Clarke. Epitaxial co-au superlattices. *Phys. Rev. Lett.*, 62:653, 1989.
- [83] J. Brandenburg, R. Hühne, L. Schultz, and V. Neu. Domain structure of epitaxial co films with perpendicular anisotropy. *Phys. Rev. B*, 79:054429, 2009.
- [84] F.J.A. den Broeder, D. Kuiper, A.P. van de Mosselaer, and W. Hoving. Perpendicular magnetic anisotropy of co-au multilayers induced by interface sharpening. *Phys. Rev. Lett.*, 60:2769, 1988.
- [85] H. Yamane, Y. Maeno, and M. Kobayashi. Annealing effects on co/noble metal multilayer films. *J. Magn. Magn. Mat.*, 126:320–322, 1993.
- [86] G. Gubbiotti, G. Carlotti, F. Albertini, F. Casoli, E. Bontempi, L.E. Depero, H. Kood, and R.D. Gomez. Influence of annealing on co/au multilayers: a structural and magnetic study. *Thin Solid Films*, 428:102, 2003.
- [87] A. Kirilyuk, A. V. Kimel, and Th. Rasing. Ultrafast optical manipulation of magnetic order. *Rev. Mod. Phys.*, 82:2731, 2010.
- [88] D. Rudolf, Chan La-O-Vorakiat, M. Battiato, R. Adam, J. M. Shaw, E. Turgut, P. Maldonado, S. Mathias, P. Grychtol, H. T. Nembach, T. J. Silva, M. Aeschlimann, H. C. Kapteyn, M. M. Murnane, C. M. Schneider, and P. M. Oppeneer. Ultrafast magnetization enhancement in metallic multilayers driven by superdiffusive spin current. *Nat. Commun*, 3:1037, 2012.
- [89] B. Vodungbo et al. Indirect excitation of ultrafast demagnetization. *Sci. Reports*, 6:18970, 2016.
- [90] I. Radu, K. Vahaplar, C. Stamm, T. Kachel, N. Pontius, H. A. D'urr, T. A. Ostler, J. Barker, R. F. L. Evans, R. W. Chantrell, A. Tsukamoto, A. Itoh, A. Kirilyuk, Th. Rasing, and A. V. Kimel. Transient ferromagnetic-like state mediating ultrafast reversal of antiferromagnetically coupled spins. *Nature (London)*, 472:205–208, 2011.
- [91] T.A. Ostler, J. Barker, R.F.L. Evans, R.W. Chantrell, U. Atxitia, O. Chubykalo-Fesenko, S. El Moussaoui, L. Le Guyader, E. Mengotti, L.J. Heyderman, F. Nolting, A. Tsukamoto, A. Itoh, D. Afanasiev, B.A. Ivanov, A.M. Kalashnikova, K. Vahaplar, J. Mentink, A. Kirilyuk, Th. Rasing, and A.V. Kimel. Ultrafast heating as a sufficient stimulus for magnetization reversal in a ferrimagnet. *Nature Comm.*, 3:666, 2012.
- [92] Q. Zhang, A. V. Nurmikko, A. Anguelouch, G. Xiao, and A. Gupta. Coherent magnetization rotation and phase control by ultrashort optical pulses in cro₂ thin films. *Phys. Rev. Lett.*, 89:177402, 2002.
- [93] J.-Y. Bigot, M. Vomir, L. H. F. Andrade, and E. Beaupaire. Ultrafast magnetization dynamics in ferromagnetic cobalt: the role of anisotropy. *Chem. Phys.*, 76:137–146, 2005.
- [94] A.V. Scherbakov, A.S. Salasyuk, A.V. Akimov, X. Liu, M. Bombeck, C. Brueggeman, D.R. Yakovlev, V.F. Sapega, J.K. Furdyna, and M. Bayer. Coherent magnetization precession in ferromagnetic (ga,mn)as induced by picosecond acoustic pulses. *Phys. Rev. Lett.*, 105:117204, 2010.
- [95] L. Thevenard, E. Perrone, C. Gourdon, C. Testelin, M. Cubukcu, E. Charron, S. Vincent, A. Lemaitre, and B. Perrin. Effect of picosecond strain pulses on thin layers of the ferromagnetic semiconductor (ga,mn)(as,p). *Phys. Rev. B*, 82:104422, 2010.
- [96] J.W. Kim, M. Vomir, and J.-Y. Bigot. Ultrafast magneto-acoustics in nickel films. *Phys. Rev. Lett.*, 109:166601, 2012.
- [97] K.A. Nelson, R.J.D. Miller, D.R. Lutz, and M.D. Fayer. Optical generation of tunable ultrasonic waves. *J. Appl. Phys.*, 53(1144), 1982.
- [98] J. Janusonis, C.L. Chang, P.H.M. van Loosdrecht, and R.I. Tobey. Frequency tunable surface magneto elastic waves. *Appl. Rev. Lett.*, 106(181601), 2015.
- [99] J. Janusonis, C.L. Chang, T. Jansma, A. Gatilova, A.M. Lomonosov, V. Shalagatskyi, V.S. Vlasov, V.V. Temnov, and R.I. Tobey. Ultrafast magnetoelastic probing of surface acoustic transients. *arXiv:1601.04350*, 2016.
- [100] D. Afanasiev, I. Razdolski, K. M. Skibinsky, D. Bolotin, S. V. Yagupov, M. B. Strugatsky, A. Kirilyuk, Th. Rasing, and A. V. Kimel. Coherent magnetization rotation and phase control by ultrashort optical pulses in cro₂ thin films. *Phys. Rev. Lett.*, 112:147403, 2014.

- [101] O. Kovalenko, T. Pezeril, and V.V. Temnov. New concept for magnetization switching by ultrafast acoustic pulses. *Phys. Rev. Lett.*, 110(227201):266602, 2013.
- [102] L. Thevenard, J.-Y. Duquesne, E. Peronne, H.J. von Bardeleben, H. Jaffres, S. Ruttala, J.-M. George, A. Lematre, and C. Gourdon. Irreversible magnetization switching using surface acoustic waves. *Phys. Rev. B*, 87:144402, 2013.
- [103] V. Sampath, N. dSouza, D. Bhattacharya, G.M. Atkinson, S. Bandyopadhyay, and J. Atulasimha. Switching the magnetization of magnetostrictive nanomagnets from single-domain to non-volatile vortex states with a surface acoustic wave. *arXiv:1601.02081*, 2016.
- [104] F. Sotier, T. Thomay, T. Hanke, J. Korger, S. Mahapatra, A. Frey, K. Brunner, R. Bratschitsch, and A. Leitenstorfer. Femtosecond few-fermion dynamics and deterministic single-photon gain in a quantum dot. *Nature Physics*, 5:352 – 356, 2009.
- [105] Al. L. Efros, M. Rosen, M. Kuno, M. Nirmal, D. J. Norris, and M. Bawendi. Band-edge exciton in quantum dots of semiconductors with a degenerate valence band: Dark and bright exciton states. *Phys. Rev. B*, 54:4843, 1996.
- [106] J. Huneke, I. D’Amico, P. Machnikowski, T. Thomay, R. Bratschitsch, A. Leitenstorfer, and T. Kuhn. Role of coulomb correlations for femtosecond pump-probe signals obtained from a single quantum dot. *Phys. Rev. B*, 84:115320, 2011.
- [107] Jorge R. Zurita-Sánchez and Lukas Novotny. Multipolar interband absorption in a semiconductor quantum dot. i. electric quadrupole enhancement. *JOSA B*, 19:1355 – 1362, 2002.
- [108] T. de Roo, J. Haase, J. Keller, C. Hinz, M. Schmid, D.V. Seletskiy, H. Clfen, A. Leitenstorfer, and S. Mecking. A direct approach to organic/inorganic semiconductor hybrid particles via functionalized polyfluorene ligands. *Adv. Funct. Mater.*, 24:2714, 2014.
- [109] A. P. Alivisatos. Perspectives on the physical chemistry of semiconductor nanocrystals. *J. Phys. Chem.*, 100:13226 – 13239, 1996.
- [110] O.A. Aktsipetrov, E.M. Kim, R.V. Kapra, T.V. Murzina, A.F. Kravets, M. Inoue, S.V. Kuznetsova, M.V. Ivanchenko, and V.G. Lifshits. Magnetization-induced optical third-harmonic generation in co and fe nanostructures. *Phys. Rev. B*, 73(1):140404, 2006.
- [111] T. Hanke, G. Krauss, D. Träutlein, B. Wild, R. Bratschitsch, and A. Leitenstorfer. Efficient nonlinear light emission of single gold optical antennas driven by few-cycle near-infrared pulses. *Phys. Rev. Lett.*, 103:257404, 2009.
- [112] T. Hanke, J. Cesar, V. Knittel, A. Trügler, U. Hohenester, A. Leitenstorfer, and R. Bratschitsch. Tailoring spatiotemporal light confinement in single plasmonic nanoantennas. *Nano Lett.*, 12(2):992–996, 2012.
- [113] D. Brida, G. Krauss, A. Sell, and A. Leitenstorfer. Ultrabroadband erbium fiber lasers. *Laser and Photonics Reviews*, 8:409 – 428, 2014.